Aging impairs cold-induced beige adipogenesis and adipocyte metabolic reprogramming

Corey D. Holman[1,2], Alexander P. Sakers[1,2], Ryan P. Calhoun[1,2], Lan Cheng[1,2], Ethan C. Fein[1,2], Christopher Jacobs[3,4], Linus Tsai,[3-5] Evan D. Rosen,[3-5] and Patrick Seale[1,2]

1. Institute for Diabetes, Obesity & Metabolism; Perelman School of Medicine at the University of Pennsylvania, Philadelphia, PA, USA
2. Department of Cell and Developmental Biology; Perelman School of Medicine at the University of Pennsylvania, Philadelphia, PA, USA
3. Division of Endocrinology, Diabetes, and Metabolism, Beth Israel Deaconess Medical Center, Boston, MA, USA
4. Broad Institute of MIT and Harvard, Cambridge, MA, USA
5. Harvard Medical School, Boston, MA, USA

*Correspondence should be addressed to:

Patrick Seale
Perelman School of Medicine
University of Pennsylvania
Smilow Center for Translational Research
3400 Civic Center Blvd, Rm. 12-105
Philadelphia, PA, 19104. USA
Tel: 215-573-8856
Email: sealep@pennmedicine.upenn.edu

Abstract

The energy-burning capability of beige adipose tissue is a potential therapeutic tool for reducing obesity and metabolic disease, but this capacity is decreased by aging. Here, we evaluate the impact of aging on the profile and activity of adipocyte stem and progenitor cells (ASPCs) and adipocytes during the beiging process. We found that aging increases the expression of *Cd9* and other fibro-inflammatory genes in fibroblastic ASPCs and blocks their differentiation into beige adipocytes. Fibroblastic ASPC populations from young and aged mice were equally competent for beige differentiation *in vitro*, suggesting that environmental factors suppress adipogenesis *in vivo*. Examination of adipocytes by single nucleus RNA-sequencing identified compositional and transcriptional differences in adipocyte populations with age and cold exposure. Notably, cold exposure induced an adipocyte population expressing high levels of *de novo* lipogenesis (DNL) genes, and this response was severely blunted in aged animals. We further identified natriuretic peptide clearance receptor *Npr3*, a beige fat repressor, as a marker gene for a subset of white adipocytes and an aging-upregulated gene in adipocytes. In summary, this study indicates that aging blocks beige adipogenesis and dysregulates adipocyte responses to cold exposure and provides a unique resource for identifying cold and aging-regulated pathways in adipose tissue.

Introduction

Brown and beige fat cells are specialized to burn calories for heat production and have the capacity to reduce obesity and metabolic disease. Brown adipocytes are localized in dedicated brown adipose tissue (BAT) depots, whereas beige adipocytes develop in white adipose tissue (WAT) in response to cold exposure, and other stimuli (Wang and Seale, 2016). Adult humans possess thermogenic adipose depots that appear to resemble rodent beige adipose tissue (Jespersen et al., 2013; Wu et al., 2012). Brown and beige adipocytes share similar cellular features such as abundant mitochondria, multilocular lipid droplets, and expression of thermogenic genes like Uncoupling Protein-1 (UCP1). UCP1, when activated, dissipates the mitochondrial proton gradient, leading to high levels of substrate oxidation and heat production (Cannon and Nedergaard, 2004). Brown and beige adipocytes can also produce heat via other UCP1-independent futile cycles (Chouchani et al., 2019).

Increasing beige fat development in mice reduces obesity and improves insulin sensitivity, whereas ablation of beige fat in mice causes metabolic dysfunction (Cederberg et al., 2001; Cohen et al., 2014; Seale et al., 2011; Shao et al., 2016; Stine et al., 2016). Furthermore, transplantation of human beige adipocytes into obese mice reduces liver steatosis and improves metabolic health (Min et al 2016). Beige adipocytes develop via the *de novo* differentiation of adipocyte stem and progenitor cells (ASPCs) or through induction of the thermogenic program in adipocytes (Ferrero et al., 2020; Sakers et al., 2022; Shao et al., 2019).

Human and mouse thermogenic adipose tissue activity declines with aging, predisposing to cardiometabolic disease and limiting the potential of brown/beige fat-targeted therapies (Becher et al., 2021; Berry et al., 2017; Cypess et al., 2012; Rogers et al., 2012; Wang et al., 2019; Yoneshiro et al., 2011). In mice, beige adipose tissue is reduced by ‘middle-age’ (i.e., 1-year-old), preceding many of the damaging effects of old age on organ function (Berry et al., 2017; Goncalves et al., 2017; Rogers et al., 2012). The aging-associated decline in beige fat activity can occur independently of increases in body weight (Rogers et al., 2012; St-Onge, 2005). A variety of processes and pathways have been linked to the aging-induced deficit in beige fat formation, including diminished proliferation and cellular senescence of ASPCs (Berry et al., 2017), increased fibrosis (Wang et al., 2019), increased inflammation (Amiya Kumar Ghosh, 2019), accumulation of anti-adipogenic regulatory cells (Nguyen et al., 2021), and reduced adrenergic tone (Rogers et al., 2012). However, a comprehensive understanding of how cold exposure and aging affect ASPC identity, adipogenesis, and adipocyte phenotypic switching remains elusive.

We applied ASPC lineage tracing, along with unbiased single-cell and single-nucleus RNA sequencing (scRNA-seq; snRNA-seq) to profile the beiging process and evaluate the impact of aging on this process. We found that aging modulates the gene program of multiple fibroblastic ASPC populations and blocks the differentiation of these cells into beige adipocytes *in vivo*. snRNA-seq analysis revealed four types of adipocytes defined by different responses to cold exposure and aging: beige, *Npr3*-high, *de novo* lipogenesis (DNL)-low, and DNL-high. Notably, DNL-high adipocytes were defined by a marked induction of DNL genes during cold exposure in young compared to aged animals. A white adipocyte subpopulation in young mice was marked by expression of Natriuretic peptide receptor-3 (*Npr3*), which was also increased in adipocyte populations from aged mice. Altogether, this study shows that aging blocks cold-stimulated adipocyte reprogramming and ASPC adipogenesis, while implicating suppression of natriuretic peptide signaling and DNL as contributing to the aging-mediated decline in beige fat formation.

Results

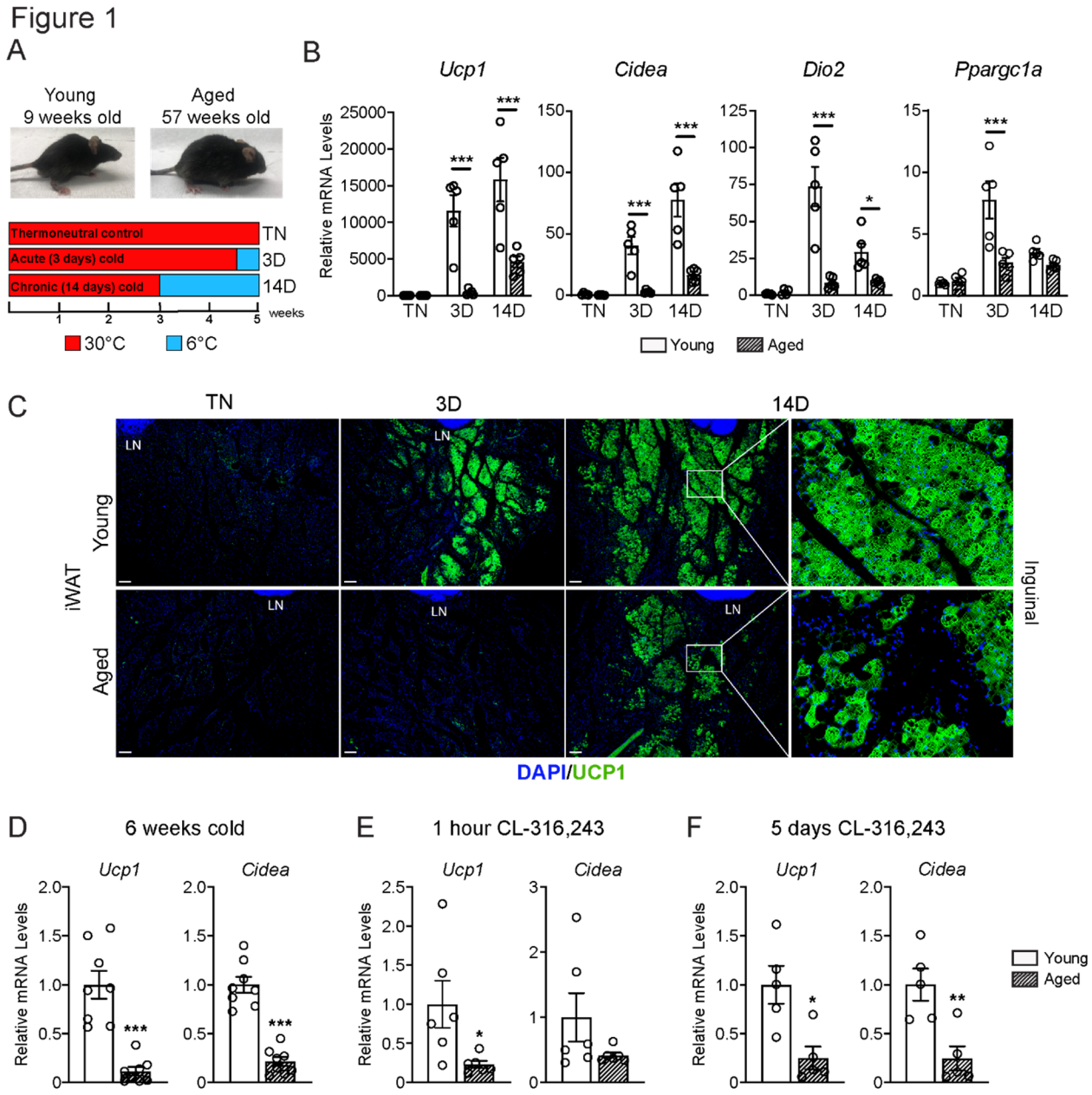

Figure 1. Aged mice exhibit decreased iWAT beiging in response to cold exposure or β3-agonist treatment. (**A**) Young (9-week-old) and aged (57-week-old) C57BL/6 mice were acclimated to 30°C for 3 weeks, followed by two additional weeks either remaining at 30°C (TN, thermoneutral controls), spending the last 3 days at 6°C (3D, acute cold) or last 14 days at 6°C (14D, chronic cold). (**B**) Relative mRNA levels of thermogenic marker genes in mouse iWAT from (A), n=5. (**C**) Immunofluorescence analysis of UCP1 (green) and DAPI (blue) in iWAT sections from mice in (A), LN = lymph node. Scale bar 100 µm. (**D-F**) Relative mRNA levels of *Ucp1* and *Cidea* in iWAT from separate groups of young and aged mice that were either: exposed to 6°C cold for 6 weeks (D), treated with CL-316,243 for 1 hour (E) or treated with CL 316,243 for 5 days (F). Data represent mean ± SEM, points represent biological replicates, 2 groups analyzed using a Student's t-test, and multiple conditions analyzed using a two-way ANOVA with a Tukey correction for multiple comparisons. Significance: not significant, P > 0.05; * P < 0.05 ** P < 0.01; *** P < 0.001.

97 **Aging impairs iWAT beiging**

98 To study the impact of aging on beige adipose tissue development, we exposed young (9-
99 week-old) and middle aged (57-week-old) C57BL/6 mice to 6°C for either 3 or 14 days. All mouse
100 groups were first acclimated to 30°C (thermoneutrality [TN]) for 3 weeks to reduce beige adipose
101 tissue to baseline (low) levels. Following acclimation, TN-housed mice remained at 30°C; acute
102 cold mice (3D) were transitioned to 6°C after 11 days for the final 3 days; and chronic cold mice
103 (14D) were moved to 6°C for two weeks (***Figure 1A***). As expected, the aged mice weighed more
104 and had larger iWAT depots than the young mice (***Figure S1A,B***). Cold exposure greatly and
105 progressively increased the expression levels of thermogenic genes *Ucp1*, *Cidea*, *Dio2* and
106 *Ppargc1a* in young iWAT, and the activation of these genes was significantly blunted in aged
107 mice, especially at the 3D time point (***Figure 1B***). Immunofluorescence (IF) staining showed a
108 robust induction of UCP1 protein in multilocular adipocytes of young iWAT at 3D of cold exposure,
109 which was further increased at 14D. The induction of $UCP1^{+}$ beige adipocytes was severely
110 reduced in aged animals, with strikingly few UCP1+ adipocytes detected. At 14D, the beige
111 adipocytes looked morphologically similar in young and aged mice, though there were fewer in
112 aged animals (***Figure 1C***). At both ages, beige adipocytes were more prominent in the inguinal
113 versus dorsolumbar region of iWAT, consistent with other reports (Barreau et al., 2016; Chi et al.,
114 2018; Dichamp et al., 2019), and beiging was largely absent in the dorsolumbar region of aged
115 mice (***Figure S1C-D, F***). To determine if the beiging response was delayed in aged mice, we
116 exposed young and aged mice at 6°C for 6 weeks. At this time point, the iWAT of aged mice
117 exhibited a larger deficit in thermogenic gene expression compared to young animals (***Figure***
118 ***1D***). Thermogenic gene levels in interscapular BAT were similar between young and aged mice,
119 at TN and after cold exposure, indicating that the inhibitory effects of aging were selective to WAT
120 (***Figure S1E***).

121 Next, we examined beige fat formation in young and aged animals upon treatment with
122 the β3-selective adrenergic agonist CL-316,243 (CL). CL acts in an adipose tissue autonomous
123 manner to stimulate beige fat biogenesis, bypassing the central nervous system pathways that
124 mediate the cold response. Acute CL treatment for only 1-hour increased *Ucp1* expression in in
125 iWAT of young mice to a much greater extent than in aged mice (***Figure 1E***). Chronic CL exposure
126 for 5 days also induced much higher expression levels of *Ucp1* and *Cidea* in iWAT of young
127 compared to aged mice (***Figure 1F***). Taken together, these results demonstrate that beige
128 adipose tissue induction is severely impaired in middle aged mice.

Figure 2

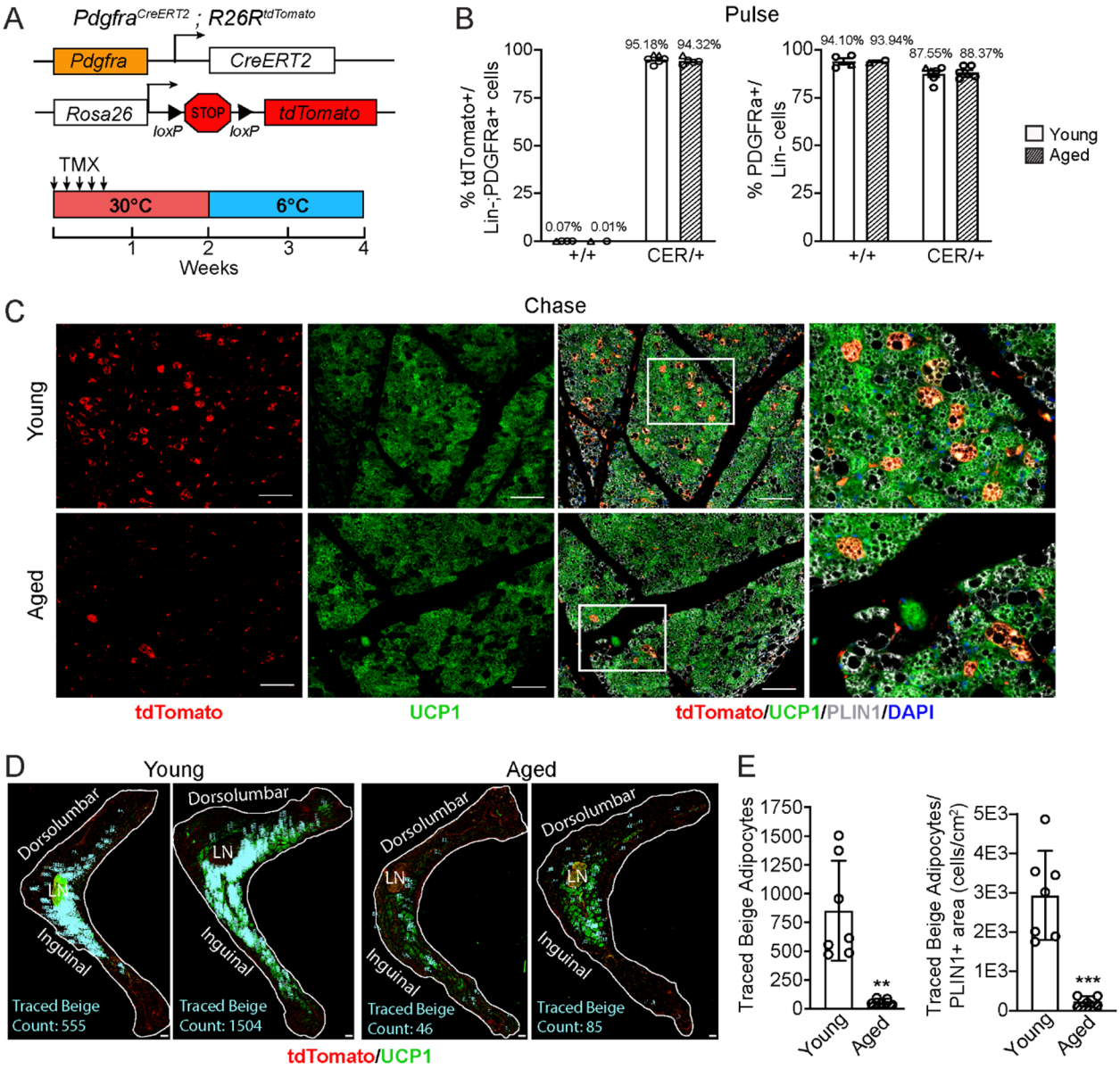

Figure 2. Aging blocks beige adipogenesis from fibroblastic ASPCs.

(**A**) Schematic of *Pdgfra*^{CreERT2};*R26R*^{tdTomato} reporter mouse model and lineage tracing paradigm. (**B**) Flow cytometry-based quantification showing proportions of tdTomato-expressing cells (as % of total Live, Lin- (CD45-/CD31-, PDGFRα^{+} cells) (left) and PDGFRα^{+} cells (as % of total Live, Lin- cells) (right) in iWAT from young and aged Cre^{-} (control, +/+), and Cre+ (CER) mice. n=6 young, 5 aged (Circles represent male mice, triangles represent female mice). (**C**) IF analysis of tdTomato (red), UCP1 (green), PLIN1 (white) and DAPI (blue) in iWAT from young and aged reporter mice after 14 days of 6°C cold exposure (chase). Scale bar 100 µm. (**D**) Representative stitched images of full length iWAT histology slices from samples in (C) showing quantification of traced tdTomato^{+}; UCP1^{+} multilocular (beige) adipocytes (blue numbers). LN= lymph node, scale bar 500 µm. (**E**) Quantification of traced beige adipocytes from (D) presented as total cell number (left) or proportion of PLIN1^{+} area (right), n=7 (young), n=5 (aged). Data represent mean ± SEM, points represent biological replicates, 2 groups analyzed using a

140 Student's t-test, and multiple conditions analyzed with a two-way ANOVA with a Tukey correction for multiple comparisons.
141 Significance: not significant, P > 0.05; * P < 0.05 ** P < 0.01; *** P < 0.001.
142

143 **Aging blocks beige adipogenesis from *Pdgfra*⁺ ASPCs**

144 To determine the contribution of fibroblastic ASPCs to beige adipocytes during cold
145 exposure, we performed lineage tracing using *Pdgfra-Cre*^{ERT2};*R26R*^{tdTomato} reporter mice. *Pdgfra*
146 expression marks multiple ASPC populations, including preadipocytes (Merrick et al., 2019;
147 Sakers et al., 2022). Young and aged reporter mice were treated with tamoxifen for 5 days at TN
148 (30°C; "pulse") to activate Cre and induce tdTomato expression in *Pdgfra*⁺ cells. Following a 9
149 day washout period, mice were transferred to 6°C (cold) for two weeks ("chase") (***Figure 2A***). We
150 observed near complete and specific labeling of ASPCs during the pulse period, with ~95% of
151 PDGFRα⁺ cells in iWAT from young and aged mice displaying tdTomato expression (***Figures 2B,***
152 ***S2A***). The proportion of PDGFRa+ cells in iWAT was similar between young and aged mice
153 (***Figure 2B***). No tdTomato-expressing adipocytes were observed after the pulse (***Figure S2B***).
154 After 14 days of cold exposure, we detected many newly developed beige adipocytes from ASPCs
155 in young mice (visible as tdTomato⁺/UCP1⁺ multilocular adipocytes). By contrast, very few ASPC-
156 derived (tdTomato⁺) adipocytes were detected in the beige fat areas of aged iWAT at day 14
157 (***Figures 2C***). Quantifying across the entire length of iWAT pads revealed that most beige
158 adipogenesis occurred in the inguinal region and was ~12-fold lower in aged compared to young
159 mice (***Figure 2D,E***). However, the overall contribution of *Pdgfra*⁺ ASPCs to beige adipocytes was
160 relatively low, even in young animals, with <20% of beige adipocytes expressing tdTomato.

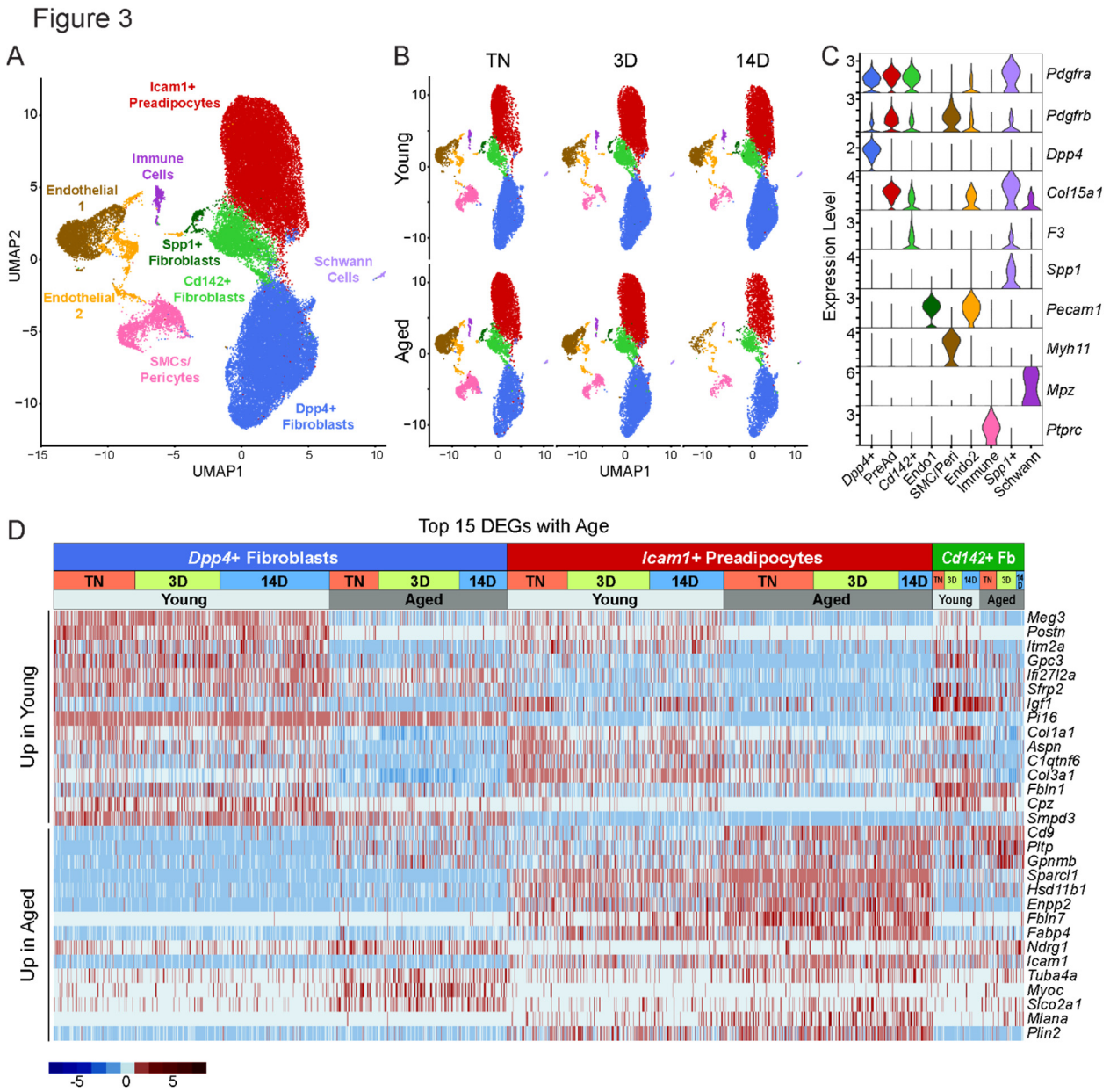

Figure 3. Single cell expression profiling of ASPCs during iWAT beiging.

(**A**) Integrated UMAP of gene expression in 54,987 stromal vascular cells (FACS depleted of CD45$^+$ immune cells) from young and aged mouse groups detailed in Figure 1A. (**B**) UMAPs split by condition. (**C**) Violin plots showing the expression levels of representative marker genes for cell clusters. Y-axis = log-scale normalized read count. (**D**) Expression heatmap of the top differentially expressed genes in young vs. aged fibroblastic ASPCs (combined *Dpp4*$^+$, preadipocytes and *Cd142*$^+$ cells). Table shows expression of these genes in ASPC populations across temperature conditions (TN, cold 3D, cold 14D) from young and aged mice.

169 **Single cell expression profiling of ASPCs**

170 We previously identified three main fibroblastic ASPC populations in iWAT: DPP4$^+$ cells,
171 ICAM1$^+$ preadipocytes, and CD142$^+$ cells. All these cell types express *Pdgfra* and have the
172 capacity to undergo adipogenic differentiation (Merrick et al., 2019). To test whether aging
173 dysregulates one or more of these ASPC types, we performed scRNA-seq on stromal vascular
174 cells from iWAT of young and aged animals, maintained at TN, or following transition to cold for
175 3 or 14 days (***Figure 1A***). ASPCs were enriched by removing immune (CD45$^+$) cells using
176 fluorescence activated cell sorting (FACS). We integrated the datasets from all conditions
177 together and performed clustering analysis. The following cell populations were annotated based
178 on their expression of cell type-specific marker genes: four fibroblast populations (*Dpp4*$^+$; *Icam1*$^+$
179 preadipocytes; *Cd142*$^+$, *Spp1*$^+$), two populations of endothelial cells (*Pecam1*$^+$); smooth muscle
180 cells/pericytes (*Myh11*$^+$, *Pdgfrb*$^+$); Schwann cells (*Mpz*$^+$); and residual immune cells (*Ptprc*$^+$)
181 (***Figures 3A-C***). We did not identify any cell population specific to either aging or cold exposure.
182 In this regard, we did not identify 'aging-dependent regulatory cells (ARCs)', which were
183 previously defined as ASPCs expressing *Lgals3* and other inflammatory genes (***Figure S3A***)
184 (Nguyen et al., 2021). The expression levels of identity markers of the ASPC populations were
185 not modulated during cold exposure or aging (***Figure S3B***).

186 Differential gene expression analyses identified aging-modulated genes in ASPCs (***Figure***
187 ***3D***). Notably, expression of *Cd9*, previously identified as a fibrogenic marker, was upregulated
188 with age in *Dpp4*$^+$ cells and preadipocytes (Marcelin et al., 2017). *Pltp* and *Gpnmb* were also
189 elevated by aging across all ASPC populations and temperature conditions. Genes
190 downregulated by aging in all ASPC populations included *Meg3*, *Itm2a* and *Gpc3 and Postn*. Of
191 note, *Postn* encodes an extracellular matrix protein that was previously reported to regulate
192 adipose tissue expansion and decrease in expression during aging (Graja et al., 2018).

Figure 4

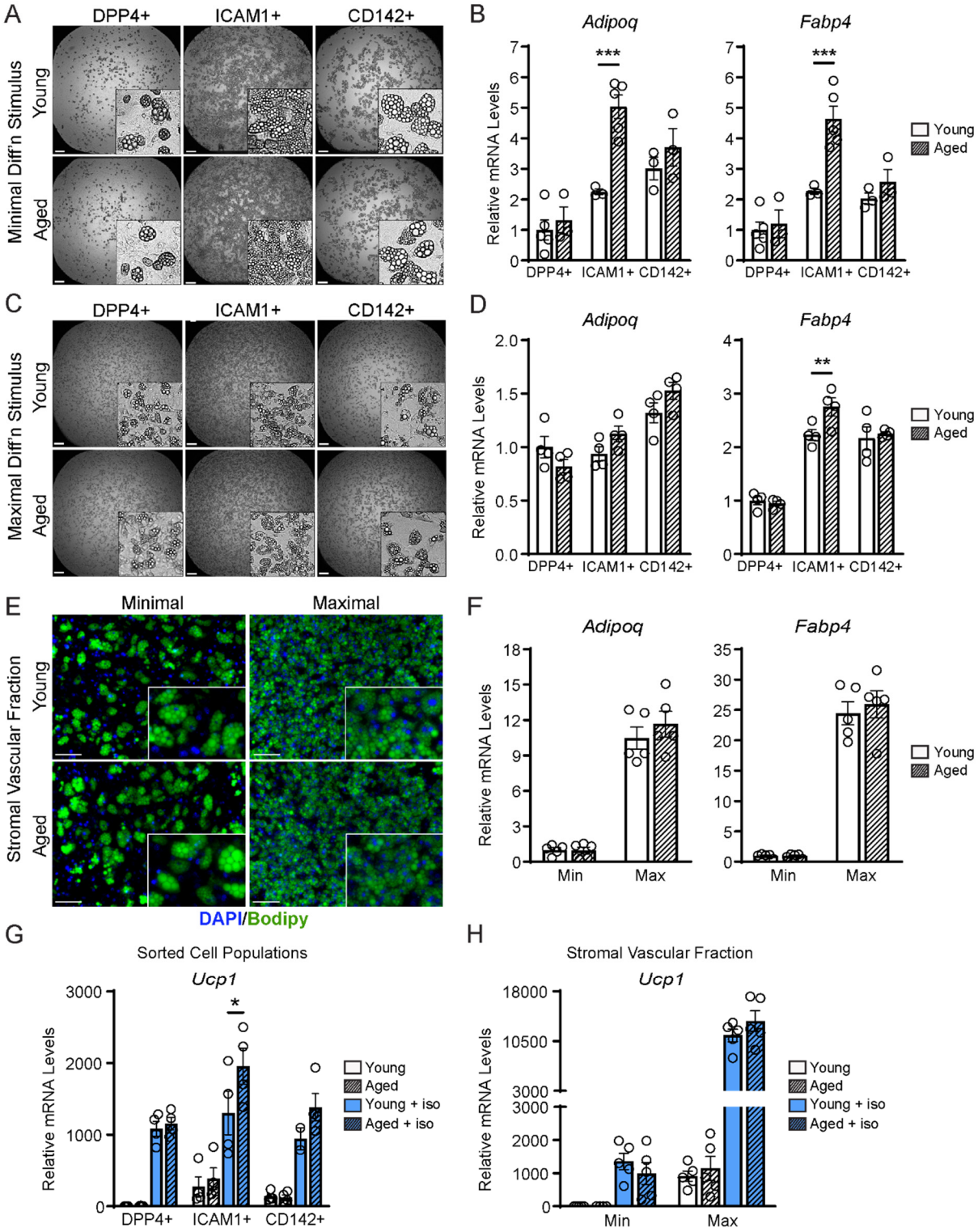

Figure 4. ASPCs from young and aged mice display similar beige adipogenic activity *ex vivo*. (**A, C**) Phase contrast images of DPP4⁺, ICAM1⁺ and CD142⁺ cells from iWAT of young and aged mice that were induced to undergo adipocyte differentiation with minimal (Min, A) or maximal (Max, C) induction cocktail for 8 days. Scale bar 200 µm. (**B, D**) mRNA levels of adipocyte marker genes *Adipoq* and *Fabp4* in cultures from (A, C). Data points represent separate wells, sorted from a pool

198 of 5 mice (A) or sorted from two pools of 2-3 mice (C). (**E**) Stromal vascular fraction (SVF) cell cultures from the iWAT of young
199 and aged mice were induced to differentiate for 8 days with Minimal or Maximal cocktail, followed by Bodipy (green) staining
200 of lipid droplets and DAPI (blue) staining of nuclei. Scale bar 100 µm. (**F**) Relative mRNA levels of *Adipoq* and *Fabp4* in
201 cultures from (E). Data points represent wells from individual mice, n = 5. (**G, H**) Relative mRNA levels of *Ucp1* in adipocyte
202 cultures from (C, E) with or without treatment with isoproterenol for 4 hours. Data points represent wells sorted from two pools
203 of 2-3 mice (G) or wells from individual mice, n=5 (H). Data represent mean ± SEM, 2 groups analyzed using a Student's t-
204 test, and multiple conditions analyzed with a two-way ANOVA with a Tukey correction for multiple comparisons. Significance:
205 not significant, $P > 0.05$; * $P < 0.05$ ** $P < 0.01$; *** $P < 0.001$.
206

207 **ASPCs from aged mice are competent for beige adipogenesis *ex vivo***

208 We next evaluated if ASPCs from young and aged animals exhibit cell-autonomous
209 differences in adipogenic differentiation capacity. We FACS-purified DPP4$^+$, ICAM1$^+$ and CD142$^+$
210 cells from the iWAT of young and aged mice, plated them in culture and induced adipocyte
211 differentiation. Using a minimal differentiation stimulus consisting of insulin only (Min), ICAM1$^+$
212 and CD142$^+$ cells underwent more efficient differentiation into lipid droplet-containing adipocytes,
213 and expressed higher levels of adipocyte genes (*Adipoq* and *Fabp4*) than DPP4$^+$ cells, consistent
214 with prior work (***Figures 4A,B***) (Merrick et al., 2019). DPP4$^+$ and CD142$^+$ cells from young and
215 aged mice underwent adipocyte differentiation and induced adipocyte genes with equivalent
216 efficiency. Unexpectedly, ICAM1$^+$ cells from aged mice exhibited greater differentiation capacity
217 than those from young mice, as evidenced by higher expression levels of *Adipoq* and *Fabp4*
218 (***Figures 4A,B***). Maximal stimulation with a full cocktail of adipogenic inducers (Max) produced
219 similar and robust differentiation in all ASPC populations from young or aged mice (***Figures***
220 ***4C,D***). To assess whether young and aged ASPCs behave differently when cultured as a mixed
221 heterogeneous population, we isolated the stromal vascular fraction (SVF) for adipogenesis
222 assays. Again, SVF cell cultures from young and aged mice displayed similar adipogenic
223 differentiation efficiency following either Min or Max stimulation (***Figures 4E,F***). Finally, we treated
224 differentiated adipocyte cultures with the pan-adrenergic agonist isoproterenol for 4 hours to
225 evaluate thermogenic gene activation (i.e., beiging). Basal levels of *Ucp1* expression were lower
226 in DPP4$^+$ cells compared to other ASPC types, but all ASPC populations activated *Ucp1*
227 expression to high and similar levels in response to isoproterenol treatment, and did not differ by
228 age (***Figure 4G***). We also did not observe an aging-related difference in the levels of *Ucp1*
229 induction in SVF-derived adipocyte cultures (***Figure 4H***). Together, these data suggest that the
230 beige adipogenic capacity of ASPCs is not intrinsically compromised in aged mice, and therefore
231 the *in vivo* deficit in beige adipogenesis could be due to non-ASPC-autonomous effects.

Figure 5

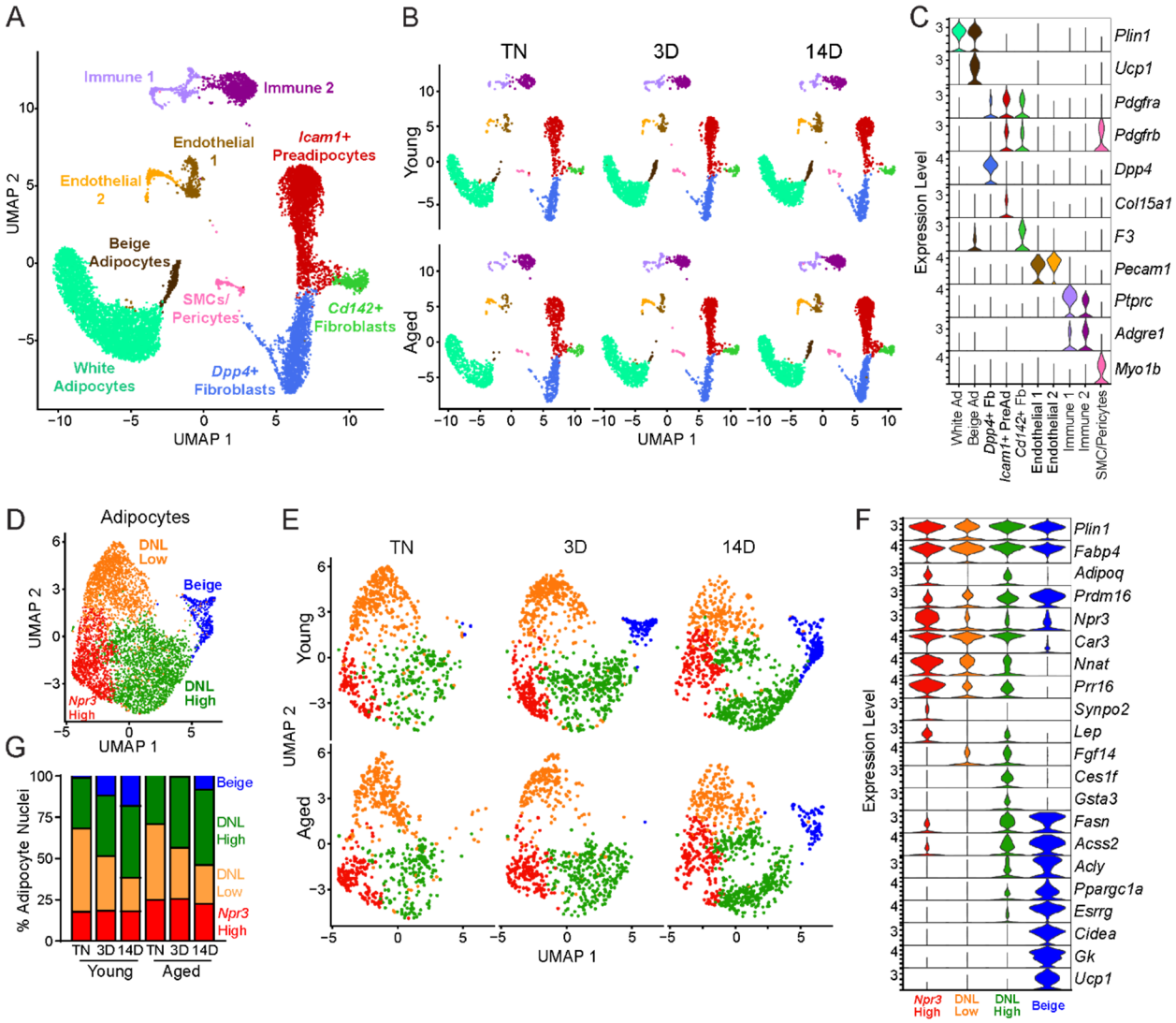

Figure 5. Single nucleus expression profiling of adipocytes during the beiging process in young and aged mice. (**A**) Fully integrated UMAP of mRNA levels in 11,905 nuclei from iWAT of mouse groups detailed in Figure 1A, n=2 mice per condition. (**B**) UMAPs split by condition. (**C**) Violin plots showing expression patterns of cell cluster-selective marker genes, Y-axis = log-scale normalized read count. (**D**) UMAP of gene expression in re-integrated adipocyte clusters including 4,937 nuclei from (A) identifying four populations: *Npr3*-high, beige, DNL-low, and DNL-high. (**E**) Adipocyte UMAPs split by condition. (**F**) Violin plots showing expression patterns of selected genes in adipocyte populations, Y-axis = log-scale normalized read count. (**G**) Adipocyte nuclei numbers in each sample, plotted as percent of total adipocytes captured for that sample.

240 **Single nucleus RNA sequencing uncovers adipocyte heterogeneity**

241 To determine the effects of aging and cold exposure on adipocyte gene profiles, we
242 performed snRNA-seq analyses of iWAT samples using the same experimental paradigm
243 described above (***Figure 1A)***. We integrated all the conditions together for analyses from two
244 separate runs. Similar cell types were captured as with scRNA-seq (***Figure 3A***), but with the
245 addition of mature adipocyte populations (***Figure 5A***). This dataset also has increased
246 representation from immune cells since there was no negative selection against $CD45^+$ cells. As
247 with the single-cell data set, we did not identify any aging-specific cell populations (***Figure S4A***).
248 However, we observed striking gene expression differences in the adipocyte cluster across age
249 and temperature. Most obvious, and expectedly, was the emergence and expansion of a distinct
250 beige adipocyte population, marked by expression of *Ucp1* and other thermogenic genes, during
251 cold exposure (***Figure 5B***).

252 To focus on adipocyte responses, we reintegrated the snRNA-seq data using only the
253 adipocytes, which revealed four main clusters (***Figures 5D-F***). All adipocyte clusters displayed
254 similarly high mRNA levels of canonical adipocyte markers *Fabp4* and *Plin1*. Beige adipocytes,
255 marked by high expression of many thermogenic genes (i.e., *Ppargc1a*, *Esrrg*, *Cidea*, *Gk, Prdm16*
256 and *Ucp1*), were the most distinctive cluster and were largely absent at TN in young and aged
257 mice. These cells began to appear in young mice after 3 days of cold exposure, and were further
258 increased at 14 days. By contrast, in aged mice, beige cells were barely detectable at 3 days of
259 cold exposure and were present at greatly reduced numbers than in young mice at 14 days
260 (***Figure 5E***). This analysis also revealed three sub-populations of 'white' adipocytes. '*Npr3*-high'
261 adipocytes were enriched for expression of *Npr3*, *Synpo2*, *Prr16*, and *Tshr*, expressed higher
262 levels of white fat marker genes *Leptin* (*Lep*) and *Nnat*, and exhibited the lowest expression levels
263 of thermogenic (beige) genes (Gesta et al., 2007; Rosell et al., 2014). Two additional white
264 adipocyte clusters were designated as '*de novo* lipogenesis (DNL)-low' and 'DNL-high' cells, both
265 of which expressed lower levels of *Npr3* and shared selective expression of *Fgf14.* DNL-high cells
266 uniquely expressed *Ces1f* and *Gsta3* and *activated* high levels of DNL pathway genes (i.e., *Fasn*,
267 *Acss2* and *Acly*) upon cold exposure (***Figure 5F***). Interestingly, Adiponectin (*Adipoq*) was
268 differentially expressed across adipocyte clusters, with higher levels in *Npr3*-high and DNL-high
269 cells. Quantification of adipocyte nuclei from this data set suggested that the proportions of *Npr3*-
270 high and DNL-high adipocytes remain stable across temperature, with aged mice having more
271 *Npr3*-high adipocytes. The proportion of beige adipocytes increased during cold exposure, while
272 DNL-low adipocytes decreased with cold exposure in both young and aged mice (***Figure 5G***).

Figure 6

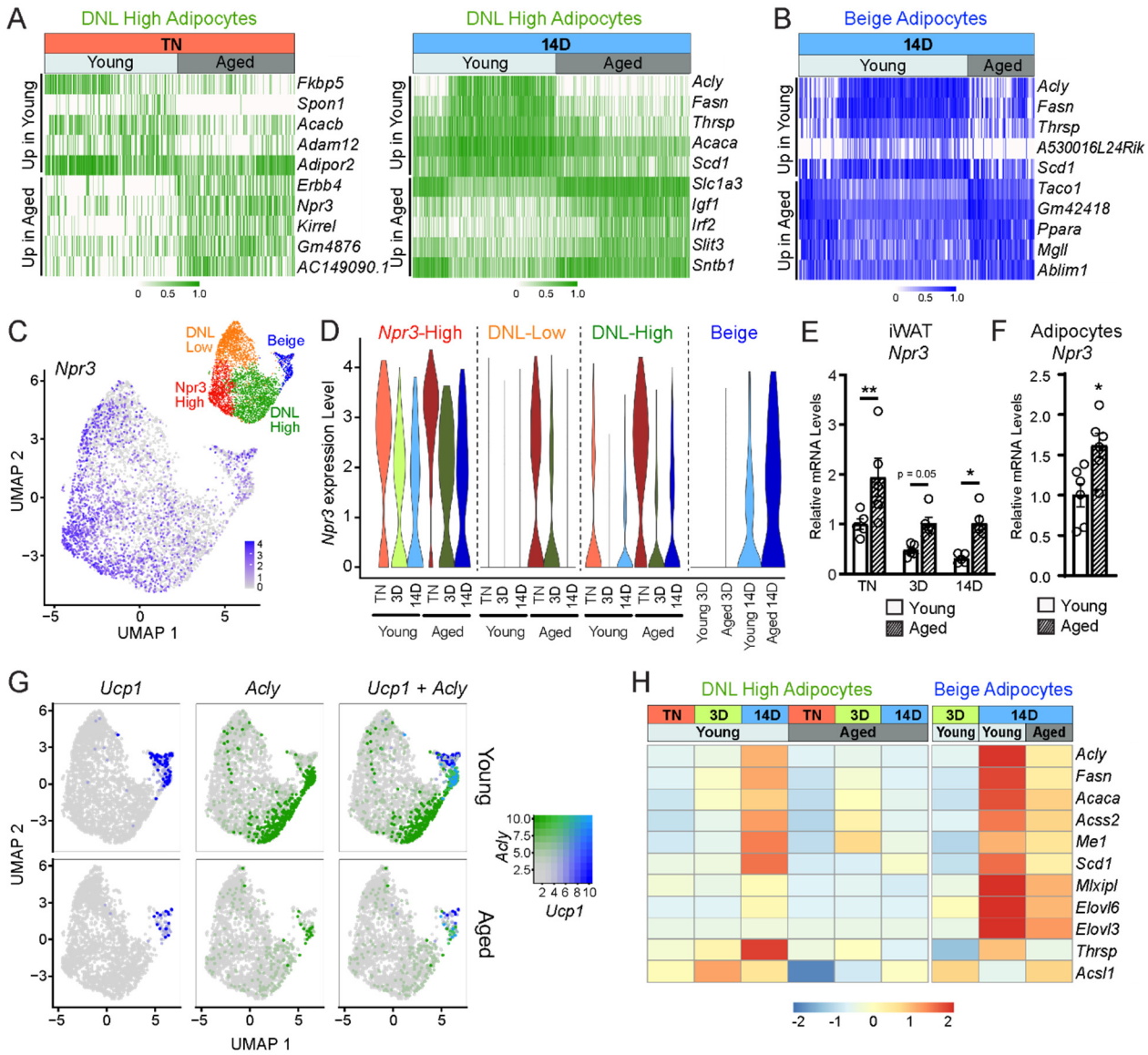

Figure 6. Aging blocks activation of the lipogenic gene program in adipocytes. (**A**) Expression heatmap of the top aging-regulated genes in DNL-high adipocytes at TN (left) and after 14 d of cold exposure (right). (**B**) Expression heatmap of the top aging-regulated genes in beige adipocytes after 14 d of cold exposure. (**C**) UMAP of *Npr3* mRNA levels in adipocyte populations (from Figure 5D). (**D**) Violin plots showing *Npr3* mRNA levels in adipocyte populations at TN (T), and at 3 and 14 days of cold exposure, Y-axis = log-scale normalized read count. (**E**) *Npr3* mRNA levels in iWAT from mouse groups described in Figure 1A, n=5. (**F**) *Npr3* mRNA levels in isolated adipocytes from TN- acclimated young and aged mice, n=6. (**G**) UMAPs of *Ucp1, Acly,* and their co-expression in adipocyte populations from young and aged mice. (**H**) Heatmap showing average expression of DNL genes in all nuclei from DNL-high and beige adipocytes per condition indicated in the top table. Data represent mean ± SEM, points represent biological replicates, 2 groups analyzed using a Student's t-test, and multiple conditions analyzed with a two-way ANOVA with a Tukey correction for multiple comparisons. Significance: not significant, P > 0.05; * P < 0.05 ** P < 0.01; *** P < 0.001.

286 **Aging dysregulates gene programming in adipocyte populations**

287 To evaluate the global effects of cold exposure and aging on adipocytes, we performed
288 differential gene expression analysis between young and aged adipocytes within each cluster.
289 DNL-high and beige adipocytes exhibited the most dramatic expression changes between young
290 and aged animals (***Figures 6A-B, S4B-C***). At TN, DNL-high cells from aged animals expressed
291 lower levels of several genes, including *Fkbp5*, *Spon1* and *Adam12.* Interestingly, *Npr3*, in
292 addition to marking *Npr3*-high cells, was increased by aging in DNL-high adipocytes and to a
293 lesser extent in other adipocyte populations (***Figure 6C,D***). In young animals, *Npr3* expression
294 was downregulated by cold exposure in the three white adipocyte populations, and this
295 downregulation was blunted in aged animals (***Figure 6D***). Gene expression analysis of whole
296 iWAT pads confirmed that *Npr3* mRNA levels were progressively decreased by cold exposure
297 and elevated in aged versus young mice under all temperature conditions (***Figure 6E***). *Npr3*
298 expression levels were also increased in isolated primary adipocytes from aged relative to young
299 mice (***Figure 6F***). Expression levels of the G-protein coupled NP receptors *Npr1* or *Npr2* were
300 not modulated by cold or aging in iWAT or iWAT adipocytes ***(Figure S4D,E)****.*

301 We also observed a striking activation of the DNL gene program (*Acly*, *Fasn*, *Acaca*, *Scd1*,
302 etc.) in DNL-high and beige adipocytes during cold exposure (***Figures 6G,H***). The induction of
303 these genes during cold exposure, exemplified by *Acly* expression, was a cluster-defining attribute
304 of DNL-high cells, which did not express beige markers like *Ucp1* even after 14 days of cold
305 exposure. Of note, we found two types of beige (*Ucp1*$^{+}$) adipocytes, distinguished by the presence
306 vs. absence of high DNL gene levels (i.e., *Ucp1*$^{+}$; DNL^{+} and *Ucp1*$^{+}$;DNL($^{-}$)), with the latter arising
307 first during cold exposure (3D vs. 14D) (***Figures 6G, S4F,G***). Importantly, the induction of DNL
308 genes was nearly completely blocked in DNL-high cells and reduced in beige cells of aged
309 animals (***Figure 6G***). Indeed, the top aging downregulated genes in adipocytes from cold exposed
310 mice correspond to DNL and related pathways, especially in DNL-high cells (***Figure S4I)***. Lastly,
311 at the whole tissue level, we observed robust induction of *Acly* in iWAT of young relative to aged
312 mice with increasing duration of cold exposure (***Figure S4H***). Taken together, these results
313 implicate the suppression of natriuretic peptide signaling and DNL in the aging-related impairment
314 of beige fat formation.

315 **Discussion**

316 Thermogenic adipose tissue activity declines during aging of mice and humans,
317 correlating with increases in fat mass and susceptibility to cardiometabolic diseases (Berry et al.,
318 2017; Cypess et al., 2009; Pfannenberg et al., 2010; Rogers et al., 2012; Saito et al., 2009; Wang
319 et al., 2019; Yoneshiro et al., 2011). Our study provides a comprehensive unbiased profile of the
320 adipose tissue beiging process and reveals pathways dysregulated by aging in ASPCs and
321 adipocytes.

322 Beige adipocytes develop via the *de novo* differentiation of ASPCs or through activation
323 of the thermogenic gene program in mature adipocytes. Previous studies defined three
324 populations of fibroblastic ASPCs in iWAT, namely *Dpp4*$^+$ cells, *Icam1*$^+$ preadipocytes, and
325 *Cd142*$^+$ cells. Aging or cold exposure did not induce dramatic shifts in either the proportions, or
326 gene expression signatures of any of these ASPC types, suggesting that these cell populations
327 are stably maintained across a range of conditions. In support of this, aging did not diminish the
328 cell-intrinsic adipogenic capacities of these ASPC populations, when subjected to adipogenesis
329 assays *ex vivo*. Notably, we did not observe the emergence of aging-dependent regulatory cells
330 (ARCs), previously described as modulated ASPCs co-expressing ASPC and immune marker
331 genes, which have the capacity to suppress adipocyte differentiation (Nguyen et al., 2021).
332 However, we did observe the induction of ARC-selective gene markers (i.e., *Lgals3*, *Cd36*)
333 specifically in immune cells (*Ptprc*$^+$, *Adgre1*$^+$) from aged mice in both our scRNA-seq and snRNA-
334 seq datasets. This *Lgals3*/*Cd36* gene signature has also been described in Lin$^+$ macrophages
335 and CD45$^+$ lipid-associated (LAM) macrophages (Burl et al., 2018; Jaitin et al., 2019). Overall,
336 our results suggest that aging-induced alterations to the systemic milieu or adipose tissue
337 environment are responsible for the block in beige adipogenesis.

338 Gene expression analyses identified several genes that were altered by aging across
339 multiple ASPC types and temperature conditions. The top aging-upregulated gene was *Cd9*,
340 which was previously identified as a marker of fibrogenic (fibrosis-generating) progenitor cells
341 (Marcelin et al., 2017). *Cd9* encodes for a tetraspanin protein implicated in various processes that
342 could affect adipogenesis, including extracellular vesicle production, cell adhesion, inflammation,
343 and platelet activation (Brosseau et al., 2018). Aging also upregulated the expression of *Pltp* and
344 *Gpnmb*, which are both linked to the regulation of inflammation and fibrosis (Prabata et al., 2021;
345 Saade et al., 2021). Conversely, *Meg3*, *Itm2a* and *Postn* were consistently downregulated across
346 all ASPC populations from aged versus young mice. Of note, Periostin (*Postn*) is an extracellular
347 matrix protein that regulates adipose tissue lipid storage, and its levels were previously shown to
348 decrease in several adipose tissue depots during aging (Graja et al., 2018).

349 We were surprised by the limited (<20%) contribution of fibroblastic (*Pdgfra*$^+$) ASPCs,
350 (which includes *Pparg*-expressing preadipocytes), to beige adipocytes during cold exposure. Of
351 note, we also observed tdTomato$^+$, unilocular white adipocytes upon cold exposure, suggesting
352 the bi-potential fate of *Pdgfra*$^+$ cells. Previous studies in mice using an adipocyte fate tracking
353 system show that a high proportion of beige adipocytes arise via the *de novo* differentiation of
354 ASPCs as early as 3 days of cold (Wang et al., 2013). However, the relative contribution from
355 ASPC differentiation and direct adipocyte conversion to the formation of beige adipocytes
356 depends highly on the experimental conditions, especially cold exposure history (Shao et al.,
357 2019). Mice housed at TN from birth undergo high rates of *de novo* beige adipogenesis upon first
358 cold exposure, whereas mice reared at room temperature acquire many 'dormant' beige
359 adipocytes that can be re-activated by cold exposure (Rosenwald et al., 2013; Shao et al., 2019).
360 Based on these findings, we presume that mature (dormant beige) adipocytes serve as the major
361 source of beige adipocytes in our cold-exposure paradigm. However, long-term cold exposure
362 also recruits smooth muscle cells to differentiate into beige adipocytes; a process that we did not
363 investigate here (Berry et al., 2016; Long et al., 2014; McDonald et al., 2015; Shamsi et al., 2021).
364 The beiging process is associated with a dramatic remodeling of adipose tissue structure
365 and metabolic function. We applied snRNA-seq analysis to investigate the cold response of iWAT
366 adipocytes in young and aged animals, leading us to identify four adipocyte clusters: beige
367 adipocytes and three "white" subsets: *Npr3*-high, DNL-low and DNL-high adipocytes. *Npr3*-high
368 adipocytes were enriched for expression of white fat-selective genes and exhibit the lowest levels
369 of thermogenic genes (Rosell et al., 2014; Ussar et al., 2014). Interestingly, *Npr3* also upregulated
370 by aging in all white adipocytes. Previous studies show that obesity also increases *Npr3* levels in
371 adipose tissue of mice and humans (Gentili et al., 2017; Kovacova et al., 2016). NPR3 represses
372 beige fat development and adipocyte thermogenesis by functioning as a clearance receptor for
373 natriuretic peptides (NPs), thereby reducing their lipolytic and thermogenic effects (Bordicchia et
374 al., 2012; Coue et al., 2018; Moro et al., 2004; Sengenès et al., 2000; Sengenes et al., 2003).
375 Together, these results suggest that *Npr3*-high adipocytes may impede beige fat development in
376 a cell non-autonomous manner by reducing NP signaling. Moreover, high NPR3 levels in aged
377 animals could contribute to the block in beige fat development, and targeting this pathway may
378 be a promising avenue to elevate beige fat activity.
379 We were also intrigued by the dramatic induction of DNL genes in beige adipocytes and
380 DNL-high cells during cold exposure. Previous work established that cold stimulates opposing
381 pathways of lipid oxidation and lipogenesis in thermogenic fat tissue (Mottillo et al., 2014;
382 Sanchez-Gurmaches et al., 2018; Yu et al., 2002). The co-occurrence of these two processes is

383 unusual and may provide a mechanism to ensure the continued availability of fatty acids to fuel
384 thermogenesis and/or provide critical metabolic intermediates, such as acetyl-CoA. The
385 Granneman lab demonstrated that high expression of the lipid catabolic enzyme MCAD and
386 lipogenic enzyme FAS occurred in separate populations of iWAT adipocytes upon stimulation with
387 a β3-adrenergic agonist for 3-7 days (Lee et al., 2017). We identified two subsets of UCP1$^+$ beige
388 adipocytes, distinguished by the presence vs. absence of high levels of DNL genes (i.e., *Ucp1*$^+$;
389 DNL-high and *Ucp1*$^+$; DNL-low). Interestingly, the *Ucp1*$^+$; DNL-high cells accumulated later during
390 cold exposure (14D), suggesting that fully cold-adapted beige adipocytes express both pathways
391 simultaneously. Of note, the induction of *Acly* and other lipogenic genes was very severely
392 impaired in aged animals. Related to this point, Martinez Calejman and colleagues showed that
393 *Acly* deficiency in brown adipocytes caused a whitened phenotype, coupled with an unexpected
394 and unexplained reduction in *Ucp1* expression (Martinez Calejman et al., 2020). We speculate
395 that high levels of ACLY may be required to support thermogenic gene transcription by supplying
396 and efficiently shuttling acetyl-CoA for acetylation of histones or other proteins.
397 Aging is a complex process, and unsurprisingly, many pathways have been linked to the
398 aging-related decline in beiging capacity. For example, increased adipose cell senescence,
399 impaired mitochondrial function, elevated PDGF signaling and dysregulated immune cell activity
400 during aging diminish beige fat formation (Benvie et al., 2023; Berry et al., 2017; Goldberg et al.,
401 2021; Nguyen et al., 2021). Of note, older mice exhibit higher body and fat mass, which is
402 associated with metabolic dysfunction and reduced beige fat development. While the effects of
403 aging and altered body composition are difficult to separate, previous studies suggest that the
404 beiging deficit in aged mice is not solely attributable to changes in body weight (Rogers et al.,
405 2012). Further studies, including additional time points across the aging continuum may help
406 clarify the role of aging and ascertain when beiging capacity decreases.
407 In summary, this work shows that aging impairs beige adipogenesis through non-cell-
408 autonomous effects on adipose tissue precursors and by disrupting adipocyte responses to
409 environmental cold exposure. Expression profiling at the single-cell level reveals adipocyte
410 heterogeneity, including two different types of UCP1$^+$ beige adipocytes. Finally, aging-
411 dysregulated pathways, including natriuretic peptide signaling and lipogenesis, may provide
412 promising targets for unlocking beige adipocyte development.
413
414 **Acknowledgements**
415 We thank members of the Seale lab for helpful advice and discussions.

Funding: NIH grants DK120982 and DK121801 to P.S.; T32 HD083185 to C.D.H; T32 DK007314 to E.F.; RC2 DK116691 to E.D.R.

Author Contributions: C.D.H, A.P.S, R.C. and P.S. were responsible for conceptualization and data analysis. C.D.H and P.S were responsible for writing of the manuscript. C.D.H and A.P.S conducted the majority of the experiments. R.C. and E.F. performed bioinformatics analyses. L.C. processed tissue sections for histology and performed immunostaining. C.J., L.T., and E.D.R. performed and processed the snRNA-seq experiment.

Competing Interests: The authors declare no competing interests.

Data and materials availability: scRNA-seq and snRNA-seq datasets are deposited in the Gene Expression Omnibus (GEO) under the superseries accession number GSE227441.

Data analysis pipelines used for processing of raw sequencing data, integration and clustering can be obtained from: https://github.com/calhounr/Aging-impairs-cold-induced-beige-adipogenesis-and-adipocyte-metabolic-reprogramming

431 **Supplemental Figures**

Figure S1

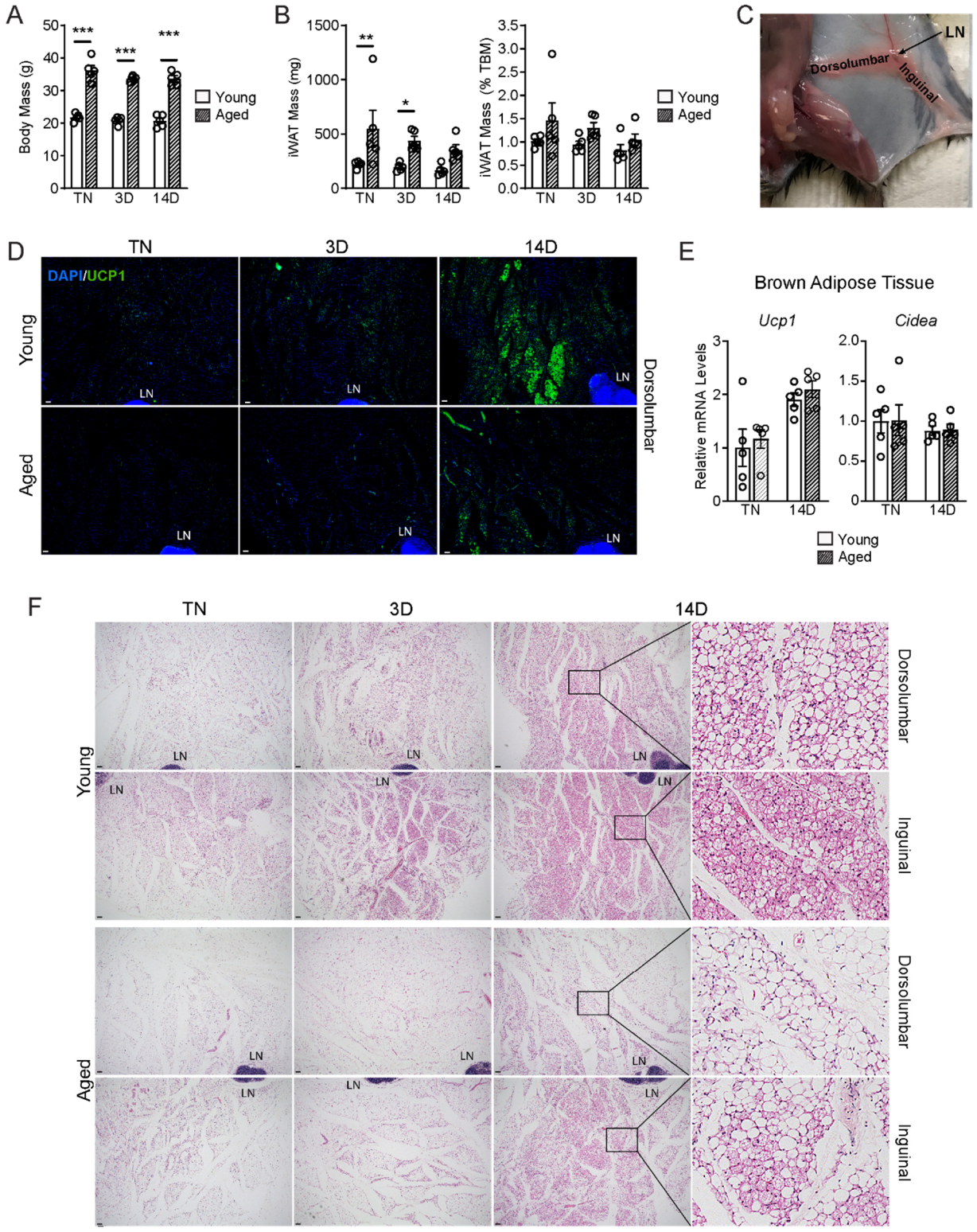

432

433 **Figure S1, related to Figure 1.** (**A-B**) Body mass and iWAT mass of mice described in Figure 1A, n=5. (**C**) Mouse dissection
434 with lymph node (LN) orientation showing the dorsolumbar and inguinal regions of the iWAT pad. (**D**) Immunofluorescence
435 analysis of iWAT with UCP1 (green) and DAPI (blue). LN=lymph node. Scale bar 100 µm. (**E**) mRNA levels of *Ucp1* and *Cidea*
436 in BAT of young and aged mice housed at TN, and either maintained at TN or exposed to cold for 2 weeks. (**F**) H&E staining
437 of serial sections of iWAT from D (above) and Figure 1C, LN=lymph node. Scale bar 100 µm. Data represent mean ± SEM,
438 points represent biological replicates, analyzed using a Student's t-test with a two-way ANOVA with a Tukey correction for
439 multiple comparisons. Significance: not significant, P > 0.05; * P < 0.05 ** P < 0.01; *** P < 0.001.
440

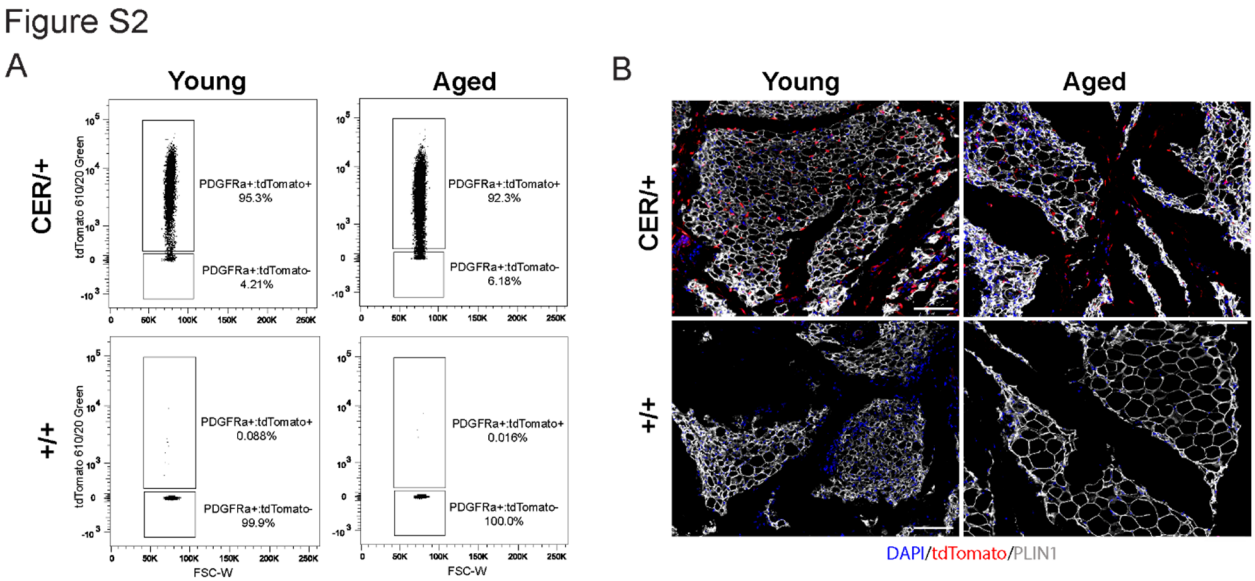

441
442 **Figure S2, related to Figure 2.** (**A**) Representative flow cytometry plots showing expression of tdTomato in gated Live, Lin$^-$;
443 PDGFRα$^+$ stromal vascular cells isolated from young and aged reporter mice (described in Figure 2) immediately after
444 treatment with tamoxifen (tmx, pulse). (**B**) Immunofluorescence analysis of iWAT from young and aged reporter mice with
445 tdTomato (red), PLIN1 (white) and DAPI (blue) after the tmx pulse, scale bar 100 µm.
446

Figure S3

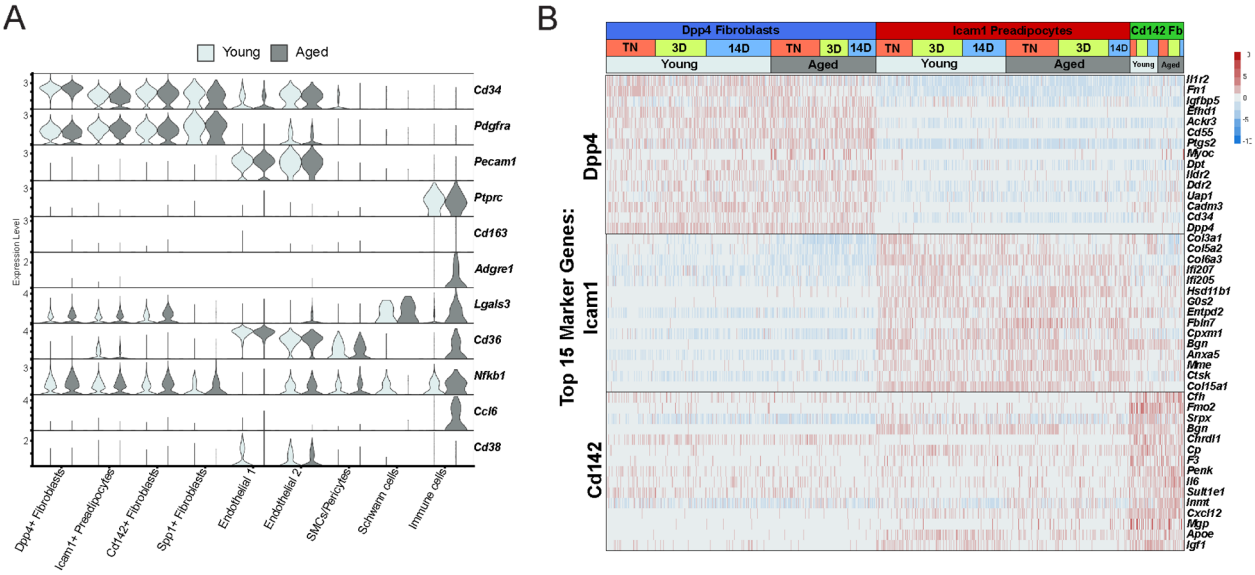

Figure S3, related to Figure 3. (**A**) Violin plot showing expression of ARC marker genes in cell clusters split by age, Y-axis = log-scale normalized read count. (**B**) Expression heatmap of top ASPC marker genes across age and housing conditions.

Figure S4

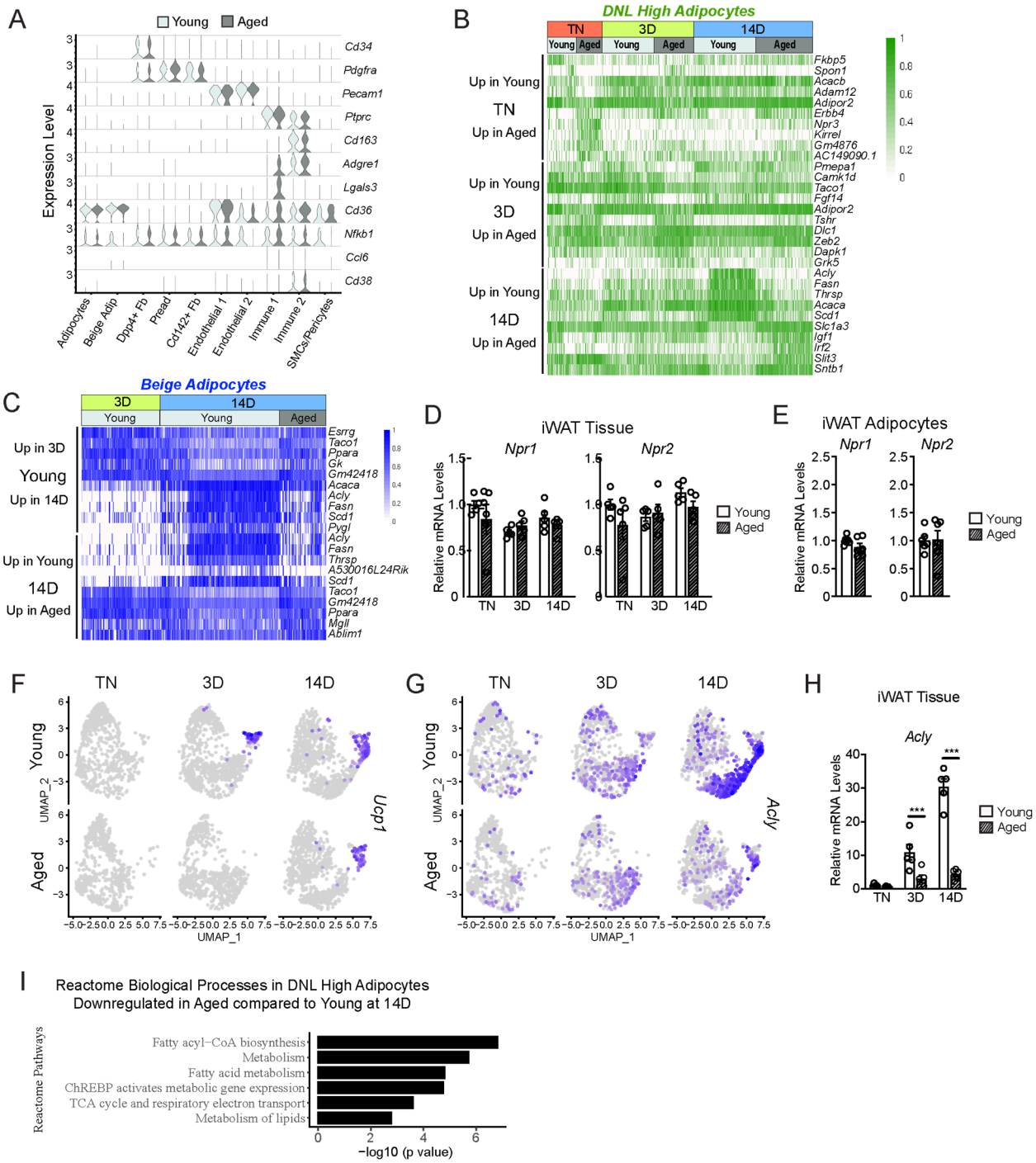

Figure S4, related to Figures 5,6. (**A**) Violin plot showing expression levels of ARC marker genes split by age, y-axis = log-scale normalized read count. (**B**) Expression heatmap of the top aging-regulated genes in DNL-high adipocytes. (**C**) Expression heatmap of the top aging-regulated and cold-regulated genes in beige adipocytes. (**D-E**) *Npr1* and *Npr2* mRNA levels in (D) iWAT from mouse groups described in Figure 1A, n=5 and (E) isolated adipocytes from iWAT from TN-acclimated young and aged mice, n=6. (**E-F**) UMAP of *Ucp1* (E) and *Acly* (F) mRNA levels in adipocyte populations (from Figure 5D). (**H**)

457 *Acly* mRNA levels in iWAT from mouse groups described in Figure 1A, n=5. (**G**) Enrichment analysis displaying the top six
458 Reactome pathways in DNL high adipocytes downregulated in aged at 14 days. Data represent mean ± SEM, points represent
459 biological replicates, 2 groups analyzed using a Student's t-test, and multiple conditions analyzed with a two-way ANOVA with
460 a Tukey correction for multiple comparisons. Significance: not significant, P > 0.05; * P < 0.05 ** P < 0.01; *** P < 0.001.
461

462 ## Materials and Methods

463 ### Key Resources Table

Reagent type (species) or resource	Designation	Source or reference	Identifiers	Additional information
genetic reagent (M. *musculus*)	C57BL/6J	The Jackson Laboratory, Bar Harbor, ME	RRID:IMSR_JAX:000664	
genetic reagent (M. *musculus*)	C57BL/6JN	NIA, Bethesda, MD	NA	
genetic reagent (M. *musculus*)	Rosa26 loxp-stop-loxp tdTomato Reporter (Ai14)	The Jackson Laboratory, Bar Harbor, ME	RRID:IMSR_JAX:007914	
genetic reagent (M. *musculus*)	Pdgfra^{CreERT2}	The Jackson Laboratory, Bar Harbor, ME	RRID:IMSR_JAX:032770	
antibody	Rabbit anti–red fluorescent protein (RFP)	Rockland, Pottstown, PA	600-401-379, RRID:AB_2209751	1:500
antibody	Rabbit anti-Perilipin (D418)	Cell Signaling, Denvers, MA	3470, RRID:AB_2167268	1:200
antibody	Rabbit anti- UCP1	Specially made by AstraZeneca, Cambridge, UK	NA	1:2000
antibody	Anti-mouse CD142	Sino Biological, Chesterbrook, PA	50413- R001	1:100
antibody	Anti-mouse CD142	R & D Systems, Minneapolis, MN	AF3178, RRID:AB_2278143	1:50
antibody	Anti-mouse CD140a-(PDGFRα)-PECy7	Biolegend, San Diego, CA	135912, RRID:AB_2715974	1:100
antibody	Anti-mouse-CD31 (APC-Fire)	Biolegend, San Diego, CA	102528, RRID:AB_2721491	1:1000
antibody	Anti-mouse CD45-allophycocyanin (APC/Cy7)	Biolegend, San Diego, CA	103116, RRID:AB_312981	1:1000
antibody	Anti-mouse ICAM1-phycoerythrin (PE/Cy7)	Biolegend, San Diego, CA	116122, RRID:AB_2715950	1:100
antibody	Anti-mouse CD26 (DPP-4)-fluorescein isothiocyanate (FITC)	Biolegend, San Diego, CA	137806, RRID:AB_10663402	1:200
sequence-based reagent	mTbp	PMID: 24703692	NA	F-GAAGCTGCGGTACAATTCCAG R-CCCCTTGTACCCTTCACCAAT
sequence-based reagent	mAdipoq	PMID: 24703692	NA	F-GCACTGGCAAGTTCTACTGCAA R-GTAGGTGAAGAGAACGGCCTTGT

sequence-based reagent	mFabp4	PMID: 24703692	NA	F-ACACCGAGATTTCCTTCAAACTG R-CCATCTAGGGTTATGATGCTCTTCA
sequence-based reagent	mCidea	PMID: 24703692	NA	F-TGCTCTTCTGTATCGCCCAGT R-GCCGTGTTAAGGAATCTGCTG
sequence-based reagent	mPgc1a	PMID: 24703692	NA	F-CCCTGCCATTGTTAAGACC R-TGCTGCTGTTCCTGTTTTC
sequence-based reagent	mUcp1	PMID: 24703692	NA	F-ACTGCCACACCTCCAGTCATT R-CTTTGCCTCACTCAGGATTGG
sequence-based reagent	mDio2	PMID: 24703692	NA	F-CAGTGTGGTGCACGTCTCCAATC R-TGAACCAAAGTTGACCACCAG
sequence-based reagent	mAcly	PMID: 31141698	NA	F-GAGTGCTATTGCGCTTCCC R-GGTTGCCGAAGTCACAGGT
sequence-based reagent	mNpr3	This Paper	NA	F-TTTTCAGGAGGAGGGGTTGC R-ACACATGATCACCACTCGCT
sequence-based reagent	mNpr1	MGH PrimerBank	Primer Bank ID: 113930717c1	F-GCTTGTGCTCTATGCAGATCG R-CCTCGACGAACTCCTGGTG
sequence-based reagent	mNpr2	MGH PrimerBank	Primer Bank ID: 118129825c2	F-CATGACCCCGACCTTCTGTTG R-CGAACCAGGGTACGATAATGCT
commercial assay or kit	ABI High-Capacity cDNA Synthesis kit	Applied Biosystems, Waltham, MA	4368813	
commercial assay or kit	Purelink RNA Mini columns	Invitrogen, Waltham, MA	LT-12183018	
commercial assay or kit	TSA TMR Tyramide Reagent Pack	Akoya Biosciences, Marlborough, MA	NEL742001KT	
commercial assay or kit	TSA Fluorescein Tyramide Reagent Pack	Akoya Biosciences, Marlborough, MA	NEL741001KT	
commercial assay or kit	Bulls Eye Decloaking Buffer	Biocare, Pacheco, CA	BULL1000 MX	
commercial assay or kit	AbC Total Antibody Compensation Bead Kit	BioLegend,San Diego, CA	A10497	
commercial assay or kit	Biotium Mix-n-Stain CF647	Sigma, Burlington, MA	MX647S100	
commercial assay or kit	PicoPure RNA Isolation Kit	Invitrogen, Waltham, MA	KIT0204	
commercial assay or kit	Qubit dsDNA High Sensitivity assay kit	ThermoFisher, Waltham, MA	Q32851	
commercial assay or kit	DNA High Sensitivity Bioanalyzer Chip (Agilent)	Agilent, Santa Clara, CA	5067-4626	
software, algorithm	Graphpad Prism	Graphpad, San Diego, CA	RRID:SCR_002798	
software, algorithm	Adobe Illustrator	Adobe, San Jose, CA	RRID:SCR_010279	
software, algorithm	Adobe Photoshop	Adobe, San Jose, CA	RRID:SCR_014199	
software, algorithm	Image J	PMID: 22743772	RRID:SCR_003070	
software, algorithm	Cell Ranger	10x Genomics	RRID:SCR_017344	
software, algorithm	Seurat	PMID: 34062119	RRID:SCR_016341	
software, algorithm	bcl2fastq	Illumina	RRID:SCR_015058	

software, algorithm	Cumulus	PMID: 32719530	RRID:SCR_021644	
software, algorithm	FACSDiva Softward	Becton Dickinson, Franklin Lakes, NJ	RRID:SCR_001456	
other	Tamoxifen (Free Base)	Sigma, Burlington, MA	T5648	
other	Corn Oil	Sigma, Burlington, MA	C8267	
other	16% Paraformaldehyde	EMS, Hatfield, PA	15710	
other	TRIzol	Invitrogen, Waltham, MA	15596018	
other	CL-316,243	Sigma, Burlington, MA	C5976	
other	4',6-Diamidine-2'-phenylindole dihydrochloride (DAPI), 1:10,000	Roche, Basel, Switzerland	10236276001	
other	Bovine Serum Albumin, fraction V, fatty-acid free	Gold Biotechnology, St. Louis, MO	A-421-250	
other	DMEM/F12	Fisher Scientific, Waltham, MA	11320033	
other	Fetal Bovine Serum	Omega Scientific, Tarzana, CA	FB-11, Lot 401714	
other	Primocin	InvivoGen, San Diego, CA	ant-pm-2	
other	PCR Master Mix, Power SYBR Green	Applied Biosystems, Waltham, MA	4367659	
other	HBSS, 1X	Fisher Scientific, Waltham, MA	14175079	
other	Dispase II	Roche, Basel, Switzerland	4942078001	
other	Collagenase, Type 1	Worthington, Lakewood, NJ	LS004197	
other	Red Blood Cell Lysis Buffer, 10x	BioLegend, San Diego, CA	420302	
other	Human Insulin, Novolin	Novo Nordisk, Bagsvaerd, Denmark	183311	
other	Dexamethasone	Sigma-Aldrich, Burlington, VT	D4902	
other	3-isobutyl-1-methylxanthine (IBMX)	Sigma-Aldrich, Burlington, VT	I7018	
other	Rosiglitazone	Cayman Chemical, Ann Arbor, MI	11884	
other	Indomethacin	Sigma-Aldrich, Burlington, VT	I8280	
other	3,30,5-Triiodo-L-thyronine sodium salt (T3)	Sigma-Aldrich, Burlington, VT	T6397	
other	isoproterenol	Sigma-Aldrich, Burlington, VT	I6504	
other	Biodipy 493/503	Invitrogen, Waltham, MA	D3922	
other	Hoechst 33342	Thermo Fisher, Waltham, MA	62249	
other	Protector RNase Inhibitor	Roche, Basel, Switzerland	3335399001	

464

465 **Mice**

466 All animal procedures were approved and performed under the guidance of the University of
467 Pennsylvania Institutional Animal Care and Use Committee. Young (4 weeks) and aged (52
468 weeks) C57BL/6 male mice were obtained from the National Institute of Aging (C57BL/6JN) or
469 Jackson Laboratories (C57BL/6J, stock number 000664). Mice were housed at 30°C for 3 weeks,
470 then were either: maintained at 30°C for 2 weeks (TN); kept at 30°C for 11 more days before
471 moving to 6°C for 3 days (3D cold) or moved to 6°C for 14 days (14D cold). Mice were single
472 housed during the final two week temperature treatment and provided with a nestlet and shepherd
473 shack. For experiments with CL316,243 (CL, Sigma-C5976), mice were housed at 30°C for 5
474 weeks, followed by intraperitoneal (IP) injection of 1 mg/kg/d CL either 1 hour prior to tissue
475 harvest or for 5 days. *Pdgfra*^{CreERT2} mice were obtained from Dr. Brigid Hogan (Duke University)
476 (Chung et al., 2018) and crossed with *Rosa26*^{tdTomato} (strain: B6.Cg-Gt(ROSA)26Sortm14(CAG-
477 tdTomato)Hze/J, stock no. 007914). To induce Cre activity, tamoxifen (Sigma, T5648) dissolved
478 in corn oil (Sigma, C8267) was injected intraperitonially (IP) into mice at a dose of 100 mg/kg/d
479 for 5 days. For all iWAT processing other than histology, the inguinal lymph node was removed.
480

481 **Histology and Immunofluorescence**

482 Tissues were fixed overnight in 4% paraformaldehyde, washed with PBS, dehydrated in ethanol,
483 paraffin-embedded and sectioned. Following deparaffinization, slides were subjected to heat
484 antigen retrieval in a pressure cooker with Bulls Eye Decloaking buffer (Biocare), unless otherwise
485 noted. Slides were incubated in primary antibody overnight and secondary antibody conjugated
486 to peroxidase and then developed using Tyramide Signal Amplification (TSA, Akoya Biosciences).
487 Samples were stained with either hematoxylin and eosin or the following antibodies: anti-red
488 fluorescent protein (RFP) (rabbit; 1:500; Rockland #600-401-379), anti-UCP1 (rabbit, 1:2000,
489 AstraZeneca), and anti-PLIN1 (rabbit, 1:200 Cell Signaling #3470). Slides were imaged on an
490 inverted fluorescence microscope (Keyence BZ-X710). For quantification of tdTomato-expressing
491 adipocytes, full-length iWAT slices were tile imaged, stitched, exported as a BigTiff, and quantified
492 using the Count Tool in Photoshop (Adobe).
493

494 **Isolation of stromal vascular cells (SCVs) and adipocytes**

495 <u>*SVCs*</u>. As previously described (Merrick et al 2019, Wang et al 2019), iWAT tissue was dissected,
496 minced gently and digested with Collagenase Type I (1.5 units/ml; Worthington) and Dispase II
497 (2.4 units/ml; Roche) in DMEM/F12 containing 1% fatty acid-free bovine serum albumin (Gold
498 Biotechnology) in a gentleMACS dissociator (Miltenyi Biotec) on program “37 MR ATDK-1.” The

499 digestion was quenched with DMEM/F12 containing 10% FBS, and the dissociated cells were
500 passed through a 100 µm filter and spun at 400 x g for 4 mins. The pellet was resuspended in red
501 blood cell lysis buffer (BioLegend), incubated for 4 mins at RT, then quenched with DMEM/F12
502 containing 10% serum. Cells were passed through a 70 µm filter, spun, resuspended, then passed
503 through a final 40 µm filter, spun at 400 x g for 4 minutes and plated or underwent further
504 processing for FACS. Mice were not pooled unless indicated.
505 *Adipocytes*. Tissue went through the same process as above, except after digestion and
506 quenching, adipocyte/SVF slurry was filtered through a 200 µm filter and centrifuged at 50 x g for
507 3 mins at RT. Using a 20 mL syringe and 1.5-inch, 25G needle, media containing the SVCs was
508 removed from below the adipocytes (and saved if concurrently isolating SVCs), leaving only the
509 adipocytes in the tube. Adipocytes were washed twice with the same media as quenching,
510 transferred to 2 mL tubes, spun a final time, media was removed from below the adipocytes again,
511 and TRIzol was added for RNA extraction. Mice were not pooled.
512
513 **FACS**
514 DPP4^{+}, ICAM1^{+}, and CD142^{+} cells were isolated as previously described (Merrick et al 2019).
515 Briefly, SVCs from the subcutaneous adipose of mice (n= 2-5) were pooled and resuspended in
516 FACS buffer (HBSS containing 3% FBS; Fisher), then incubated for 1 hr at 4°C with the following
517 antibodies: CD26 (DPP4)-fluorescein isothiocyanate (FITC) (Biolegend, 137806; 1:200), anti-
518 mouse ICAM1-phycoerythrin (PE)/Cy7 (Biolegend, 116122; 1:100), anti-mouse CD45-
519 allophycocyanin (APC)/Cy7 (Biolegend, 103116; 1:1000), anti-mouse CD31-APC-Fire
520 (Biolegend, 102528; 1:1000), and anti-mouse CD142 (Sino Biological, 50413-R001, 1:100; or
521 R&D Systems, AF3178, 1:50). Anti-mouse CD142 antibodies were conjugated with Biotium Mix-
522 n-Stain CF647 (Sigma, MX647S100). For lineage tracing pulse analysis, SVCs were isolated from
523 individual mice without pooling. SVCs were stained with anti-mouse CD31, anti-mouse CD45,
524 and anti-mouse CD140a (PDGFRA) (PE/Cy7) (Biolegend, 135912; 1:100). In all FACS
525 experiments, cells were stained with 4′,6-diamidino-2-phenylindole (DAPI) (Roche, 10236276001;
526 1:10,000) for 5 minutes, then washed three times with FACS buffer to remove unbound
527 antibodies. Cells were sorted with a BD FACS Aria cell sorter (BD Biosciences) equipped with a
528 100 µm nozzle and the following lasers and filters: DAPI, 405 and 450/50 nm; FITC, 488 and
529 515/20 nm; mTomato, 532 and 610/20 nm; PE/Cy7, 532 and 780/60 nm; CF647, 640 and 660/20
530 nm; and APC/Cy7 and APC-Fire, 640 and 780/60 nm. All compensation was performed at the
531 time of acquisition in Diva software by using compensation beads (BioLegend, A10497) for single-
532 color staining and SVCs for negative staining and fluorescence (DAPI and tdTomato).

533

534 **Cell culture and differentiation**

535 *Adipocyte precursor cells*. All cells were cultured in DMEM/F12 containing 10% FBS and Primocin
536 (50 ng/ml) (InvivoGen, ant-pm-1). DPP4$^+$, ICAM1$^+$, and CD142$^+$ populations were FACS purified,
537 plated on CellBind 384-well plates (Corning) at 15-25K cells/well, and incubated for 48 (25K cells)
538 to 72 hours (15K cells) to facilitate attachment before the induction of adipogenic differentiation.
539 For whole SVF, SVCs were isolated and plated in a 48 well CellBind plate (Corning) at a high
540 confluency of one mouse per 18 wells. No cells were passaged after plating to maintain
541 adipogenic competency. Differentiation was carried out with either maximum adipogenic cocktail,
542 max: 500 μM isobutylmethylxanthine (Sigma, I7018), 10 μM dexamethasone (Sigma, D4902),
543 125 μM indomethacin (Sigma, I8280), 1 μM rosiglitazone (Cayman Chemical, 11884), 1 nM T3
544 (Sigma, T6397), and 20 nM insulin (Novolin) or a minimal adipogenic cocktail, min: 20 nM insulin.
545 For the max adipogenic cocktail induction, cells were incubated with cocktail for 2 days and then
546 transferred to adipogenic maintenance medium for the remaining 6 days (1 μM rosiglitazone, 1
547 nM T3, and 20 nM insulin). For all conditions, medium was changed every 2 days, and cells were
548 harvested on day 8 of differentiation. For drug treatments, cells were treated for 4 hrs on day 8
549 with 1 μM isoproterenol (Sigma, I6504). Adipogenesis was assessed by staining with Biodipy
550 493/503 (Invitrogen, D3922) for lipid droplet accumulation and Hoechst 33342 (Thermo Fisher,
551 62249) for nuclei number. The cells were imaged on a Keyence inverted fluorescence microscope
552 (BZ-X710) by using DAPI (excitation, 360/40 nm; emission, 460/50 nm) and green fluorescent
553 protein (excitation, 470/40 nm; emission, 525/50 nm) filters. Individual wells were imaged in their
554 entirety at 4x magnification, and at 20x to see morphology. 384-well plates were not stained and
555 imaged in brightfield due to low cell number recovery from FACS prior to RNA extraction.

556

557 **RNA Extraction, qRT-PCR and RNA Sequencing**

558 *RNA Extraction*. Total RNA was extracted using TRIzol (Invitrogen) combined with PureLink RNA
559 Mini columns (Thermo Fisher, 12183025) for tissue and SVC cells or by PicoPure RNA Isolation
560 Kit (Applied Biosystems, KIT0204) for 384-well plate populations and adipocytes. Prior to the
561 addition of chloroform, all tissue and primary adipocytes in TRIzol included an extra spin at max
562 speed for 10 minutes at RT, then TRIzol was removed from below the lipid layer to avoid lipid
563 contamination disrupting the subsequent phase separation with chloroform. Chloroform was
564 added to the lipid-free TRIzol, spun for 15 mins at 12,000 x g and the aqueous layer was removed
565 and added to columns. mRNA was quantified using a Nanodrop and reverse transcribed to cDNA
566 using the ABI High-Capacity cDNA Synthesis kit (ABI, 4368813). Real-time PCR was performed

567 on a QuantStudio5 qPCR machine using SYBR green fluorescent dye (Applied Biosystems). Fold
568 changes were calculated using the ddCT method, with TATA binding Protein (*Tbp*) mRNA serving
569 as a normalization control.
570
571 *Single Cell RNA-seq Samples*. Cells were flow sorted to isolate live (DAPI$^-$) cells and remove
572 debris. We enriched non-immune cells by sorting out CD45$^+$ cells. Next-generation sequencing
573 libraries were prepared using the Chromium Next GEM Single Cell 3' Reagent kit v3.1 (10x
574 Genomics, 1000121) per manufacturer's instructions. Libraries were uniquely indexed using the
575 Chromium Single Index Kit T Set A, pooled, and sequenced on an Illumina NovaSeq 6000
576 sequencer in a paired-end, dual indexing run by the CHOP Center for Applied Genomics at the
577 University of Pennsylvania. Sequencing for each library targeted 20,000 mean reads per cell.
578
579 *Single Nucleus RNA-seq Samples*.
580 Nuclei were isolated from frozen mouse iWAT samples as previously described, with the following
581 modifications to integrate hash multiplexing and FANS-assisted nuclear quality thresholding and
582 sample pooling (Drokhlyansky et al., 2020; Slyper et al., 2020). Briefly, 300 mg of flash-frozen
583 adipose samples were held on dry ice until immediately before nuclei isolation, and all sample
584 handling steps were performed on ice. Each sample was placed into a gentleMACS C tube
585 (Miltenyi Biotec, 130-093-237) with 2 mL freshly prepared TST buffer (0.03% Tween 20 (Bio-Rad),
586 0.01% Molecular Grade BSA (New England Biolabs), 146 mM NaCl (ThermoFisher Scientific), 1
587 mM $CaCl_2$ (VWR International), 21 mM $MgCl_2$ (Sigma Aldrich), and 10 mM Tris-HCl pH 7.5
588 (ThermoFisher Scientific) in ultrapure water (ThermoFisher Scientific)) with 0.2 U/µL of Protector
589 RNase Inhibitor (Sigma Aldrich, RNAINH-RO). gentleMACS C tubes were then placed on the
590 gentleMACS Dissociator (Miltenyi Biotec) and tissue was dissociated by running the program
591 "mr_adipose_01" three times, and then incubated on ice for 10 minutes. Lysate was passed
592 through a 40 µm nylon filter (CellTreat) and collected into a 50 mL conical tube (Corning). Filter
593 was rinsed with 3 mL of freshly prepared ST buffer (146 mM NaCl, 1 mM $CaCl_2$, 21 mM $MgCl_2$;
594 10 mM Tris-HCl pH 7.5) with 0.2 U/µL RNase Inhibitor, and collected into the same tube. Flow-
595 through was passed through a 20 µm pre-separation filter (Miltenyi Biotec) set on top of a 5 mL
596 FACS tube (Corning) and collected into the same tube. Suspension was centrifuged in a swinging-
597 bucket centrifuge (Eppendorf) at 500 × g for 5 minutes at 4°C with brake set to low. Following
598 centrifugation, supernatant was removed and 5 mL of PBS pH 7.4 (ThermoFisher Scientific) with
599 0.02% BSA and 0.2 U/µL RNase Inhibitor was added without resuspending the nuclear pellet.
600 Sample was centrifuged again at 500 × g for 5 minutes at 4°C with brake set to low. Following

601 centrifugation, supernatant was removed, and the nuclear pellet was resuspended in 1 mL PBS-
602 0.02% BSA with 0.2 U/µL RNase Inhibitor. Each sample was split into two 500 µL aliquots and
603 transferred to new 5 mL FACS tubes for subsequent hashing. Each aliquot of resuspended nuclei
604 was stained with NucBlue (ThermoFisher, R37605), labeled with 1 µg of a unique TotalSeq anti-
605 Nuclear Pore Complex Proteins Hashtag Antibody (Biolegend), and then incubated on ice for 30
606 minutes. Suspension was centrifuged at 500 × g for 5 minutes at 4°C with brake set to low.
607 Following centrifugation, 450 µL of supernatant was removed and the nuclear pellet was
608 resuspended in 450 µL PBS-0.02% BSA with 0.2 U/µL RNase Inhibitor. For nuclear quality
609 thresholding, fluorescence-activated nuclear sorting (FANS) was implemented to collect 4,000-
610 4,300 nuclei from hashtagged aliquots directly into a shared well of a 96-well PCR plate (Thermo
611 Scientific) containing 24.6 µL of 10X RT Reagent B with 1U/uL RNase Inhibitor on a Beckman
612 Coulter MoFlo AstriosEQ fitted with a 70 µm nozzle. High-quality nuclei were selected by initial
613 gating at 360 nm with laser filter 405-448/59 followed by SSC-H and FSC-H to remove doublets
614 and unlysed cells. Once all sample aliquots were FANS-sorted, the pool of 43,000 nuclei was
615 loaded on the 10x Chromium controller (10x Genomics) according to the manufacturer's protocol.
616 cDNA and gene expression libraries were generated according to the manufacturer's instructions
617 (10x Genomics). Libraries of hashtag oligo fractions were generated according to the
618 manufacturer’s instructions (Biolegend). cDNA and gene expression library fragment sizes were
619 assessed with a DNA High Sensitivity Bioanalyzer Chip (Agilent). cDNA and gene expression
620 libraries were quantified using the Qubit dsDNA High Sensitivity assay kit (ThermoFisher,
621 Q32854). Gene expression libraries were multiplexed and sequenced on the Nextseq 500
622 (Illumina) using a 75-cycle kit and the following read structure: Read 1: 28 cycles, Read 2: 55
623 cycles, Index Read 1: 8 cycles.
624
625 **Bioinformatics analysis**
626 *Single Cell RNA Sequencing*
627 Data was processed using the Cell Ranger pipeline (10x Genomics, v.3.1.0) for demultiplexing
628 and alignment of sequencing reads to the mm10 transcriptome and creation of feature-barcode
629 matrices. The cell ranger output files were read into R (version 4.1.1) and processed utilizing the
630 standard Seurat CCA integrated workflow (version 4.3.0). Each of the six samples went through
631 a first phase of filtering, where only cells that recorded more than 200 features and only features
632 present in a minimum of 3 cells were kept. Each sample was filtered prior to downstream analysis
633 on nCount_RNA, nFeature_RNA, and mitochondrial percentages. Samples were then normalized
634 using a LogNormalization method with a scaling factor of 10000 followed by FindVariableFeatures

using Variance Stabilization Transformation with the top 6000 features to be returned. The samples were scored on their cell cycle phases which would be used in the regression later. The FindIntegrationAnchors function using the CCA reduction method and IntegrateData was utilized to integrate the data together. The integrated data-set was then scaled in which mitochondrial percentage and cell cycle state was regressed out. A principal component analysis was performed and the top 15 dimensions were kept. Uniform Manifold and Projection (UMAP) was run on the dataset, in addition to FindNeighbors and FindClusters. Differential gene expression between clusters was performed using the FindMarkers function with the Wilocox test in Seurat. Violin plots and individual UMAP plots were all generated using the Seurat toolkit VlnPlot and FeaturePlot functions, respectively. Heatmaps were generated utilizing the pheatmap package (version 1.0.12).

Single Nucleus RNA Sequencing

Raw sequencing reads were demultiplexed to FASTQ format files using bcl2fastq (Illumina; version 2.20.0). Digital expression matrices were generated from the FASTQ files using Cell Ranger (Zheng et al., 2017)(version 6.1.2) with the option to include intronic reads (--include-introns). Reads were aligned against the GRCm38 mouse genome assembly and gene counts were obtained, per-droplet, by summarizing exonic and intronic UMIs that overlapped with the GENCODE mouse annotation (release 24) for each gene symbol. In order to adjust for downstream effects of ambient RNA expression within mouse nuclei, we used the "remove-background" module from CellBender (Fleming et al., 2022) (version 0.2.0) to remove counts due to ambient RNA molecules from the count matrices and to estimate the true cells. Genes were subsequently filtered such that only genes detected in two or more cells and with at least 6 total counts (across all cells) were retained. Sample demultiplexing via hashtag oligonucleotide sequences (HTOs) was performed with the Cumulus sc/snRNA-Seq processing pipeline (Li et al., 2020). Specifically, HTO quantification was performed with the Cumulus Tool on Feature Barcoding, which provided a cell-by-HTO count matrix. This HTO count matrix, along with the gene count matrices generated via Cell Ranger (above) were used to assign each cell to their respective sample(s) with the demuxEM program. Only cells that were identified as singlets were retained (i.e. no cells identified as a multiplet or unassignable) in the per-sample CellBender-ed gene count matrices.

Cellbender output files were read into R (version 4.1.1) and processed utilizing the standard Seurat CCA and later RPCA integration workflows (version 4.3.0). Each of the hashed samples (24 in total) were merged with their respective pair to have a total of twelve samples

669 consisting of six different groups. Each sample was filtered prior to downstream analysis based
670 on their nCount_RNA, nFeature_RNA, and mitochondrial percentages. Samples were then
671 normalized using a LogNormalization method with a scaling factor of 10000 followed by
672 FindVariableFeatures using a Variance-Stabilizing Transformation as the method with the top
673 2000 features to be returned. The FindIntegrationAnchors function using the CCA reduction
674 method and IntegrateData was utilized to integrate the data together. The integrated data-set was
675 then scaled on which mitochondrial percentage was regressed. A principal component analysis
676 was performed in which only the top 18 dimensions were retained. Uniform Manifold and
677 Projection (UMAP), FindNeighbors, and FindClusters with a resolution of 0.4 was performed on
678 the dataset. To remove doublets in the dataset, we used the package scDblFinder (1.8.0) and
679 their function scDblFinder with the parameters of samples set to our twelve samples, dbr set to
680 NULL, dbr.sd set to 1, clusters set to FALSE, and multiSampleMode set to split. The object was
681 then subsetted to only contain expected singlets. Differential gene expression between clusters
682 was performed using the FindMarkers function with the Wilocox test in Seurat. Violin plots and
683 individual UMAP plots were all generated using the Seurat toolkit VlnPlot and FeaturePlot
684 functions, respectively. Heatmaps were generated utilizing the dittoSeq package (1.9.1) and
685 pheatmap package (version 1.0.12).

686 After identifying the adipocyte population, we subsetted our object on that population,
687 extracting the raw RNA counts on the cells for each of the six samples (YTN, OTN, Y3D, O3D,
688 Y14D, O14D) (Y is young, O is “Old” or as referred to in this paper, Aged). These samples were
689 then integrated together using the standard RPCA integration workflow. There was no further
690 filtering done on the reintegrated adipocyte population. Samples were normalized using a
691 LogNormalization method with a scaling factor of 10000 followed by FindvariableFeatures using
692 a Variance-Stabilizing Transformation as the method with the top 2000 features to be returned.
693 The function SelectIntegrationFeatures was performed on the dataset where it was then scaled
694 on which mitochondrial percentage was regressed, and principal components were found using
695 the ScaleData and RunPCA functions. The FindIntegrationAnchors function using the ROCA
696 reduction method and a k.anchors of 20 and IntegrateData was utilized to integrate the data
697 together. After integration, the dataset was then scaled in which mitochondrial percentage was
698 regressed on again. A principal component analysis was performed in which only the top 18
699 dimensions were retained. Uniform Manifold and Projection (UMAP), FindNeighbors, and
700 FindClusters with a resolution of 0.2 was performed on the dataset. Differential gene expression
701 between clusters was performed using the FindMarkers function with a Wilcoxon signed-rank test
702 as the method in Seurat. Violin plots and individual UMAP plots were all generated using the

703 Seurat toolkit VlnPlot and FeaturePlot functions, respectively. Heatmaps were generated utilizing
704 the dittoSeq package (1.9.1) and pheatmap package (version 1.0.12).
705 Enrichment analysis was performed on the positively expressed genes with a $\log_2$ fold
706 change (LFC) > 0.25 and a $P_{adjusted}$ value < 0.01 on comparison of the young 14 days cold and
707 old 14 days cold groups in the DNL high cluster. The generated gene list, which was in order of
708 significance, was fed into g:Profiler (version 0.2.1) using default parameters except with
709 modifications to query as an ordered query against the 'mmusculus' database, a gSCS correction
710 method for multiple testing, with domain scope set to annotated, and sources set to the Reactome
711 database. The top six enriched pathways yielded from the database were taken and displayed in
712 order of $P_{adjusted}$ value.
713
714 **Statistical methods**
715 All bar graphs represent the mean ± SEM. A Student's t-test was used when 2 groups were
716 compared. Where multiple conditions were compared, we applied two-way ANOVA with a Tukey
717 correction for multiple comparisons. Only the Young vs. Aged comparisons were depicted on
718 graphs for clarity, with additional multiple comparisons provided below. P values are indicated by
719 asterisks and defined as *p < 0.05, **p < 0.01 and ***p < 0.001. All statistics were calculated with
720 GraphPad Prism Version 10.0.3.
721

Figure	Graph	Statistical Test	Comparison	P value
1B	*Ucp1* qPCR	2 way ANOVA with a Tukey correction for multiple comparisons	3D: Young vs. Aged	<0.001
			14D: Young vs. Aged	<0.001
			Young: TN vs. 3D	<0.001
			Young: TN vs. 14D	<0.001
1B	*Cidea* qPCR	2 way ANOVA with a Tukey correction for multiple comparisons	3D: Young vs. Aged	<0.001
			14D: Young vs. Aged	<0.001
			Young: TN vs. 3D	<0.001
			Young: TN vs. 14D	<0.001
			Young: 3D vs. 14D	0.001
1B	*Dio2* qPCR	2 way ANOVA with a Tukey correction for multiple comparisons	3D: Young vs. Aged	<0.001
			14D: Young vs. Aged	0.03
			Young: TN vs. 3D	<0.001
			Young: TN vs. 14D	0.008
			Young: 3D vs. 14D	<0.001
1B	*Ppargc1a* qPCR	2 way ANOVA with a Tukey correction for multiple comparisons	3D: Young vs. Aged	<0.001
			Young: TN vs. 3D	<0.001
			Young: TN vs. 14D	0.03
			Young: 3D vs. 14D	<0.001

2B	% tdTom%/Lin-;PDGFRa+	2 way ANOVA with an Uncorrected Fisher's LSD	Young: +/+ vs. CER/+	<0.001
			Aged: +/+ vs. CER/+	<0.001
2B	% PDGFRa+/Lin- cells	2 way ANOVA with an Uncorrected Fisher's LSD	Young: +/+ vs. CER/+	0.008
4B	*Adipoq* qPCR	2 way ANOVA with a Tukey correction for multiple comparisons	ICAM1: Young vs. Aged	<0.001
			Young: DPP4 vs. CD142	0.006
			Aged: DPP4 vs. ICAM1	<0.001
			Aged: DPP4+ vs. CD142	0.004
4B	*Fabp4* qPCR	2 way ANOVA with a Tukey correction for multiple comparisons	ICAM1: Young vs. Aged	<0.001
			Aged: DPP4 vs. ICAM1	<0.001
			Aged: ICAM1 vs. CD142	0.002
4D	*Adipoq* qPCR	2 way ANOVA with a Tukey correction for multiple comparisons	Young: DPP4 vs. CD142	0.03
			Young: ICAM1 vs. CD142	0.008
			Aged: DPP4 vs. ICAM1	0.04
			Aged: DPP4 vs. CD142	<0.001
			Aged: ICAM1 vs. CD142	0.006
4D	*Fabp4* qPCR	2 way ANOVA with a Tukey correction for multiple comparisons	ICAM1: Young vs. Aged	0.008
			Young: DPP4 vs. ICAM1	<0.001
			Young: DPP4 vs. CD142	<0.001
			Aged: DPP4 vs. ICAM1	<0.001
			Aged: DPP4+ vs. CD142	<0.001
			Aged: ICAM1 vs. CD142	0.03
4F	*Adipoq* qPCR	2 way ANOVA with an Uncorrected Fisher's LSD	Young: MIN vs. MAX	<0.001
			Aged: MIN vs. MAX	<0.001
4F	Fabp4 qPCR	2 way ANOVA with an Uncorrected Fisher's LSD	Young: MIN vs. MAX	<0.001
			Aged: MIN vs. MAX	<0.001
4G	*Ucp1* qPCR	2 way ANOVA with a Tukey correction for multiple comparisons	DPP4: Young vs. Young + Iso	<0.001
			DPP4: Aged vs. Aged + Iso	<0.001
			ICAM1: Young vs. Young + Iso	<0.001
			ICAM1: Aged vs. Aged + Iso	<0.001
			ICAM1: Young + Iso vs. Aged + Iso	0.02
			CD142: Young vs. Young + Iso	0.02
			CD142: Aged vs. Aged + Iso	<0.001
			Aged + Iso: Dpp4+ vs. Icam1+	0.002
			Aged + Iso: Icam1+ vs. Cd142+	0.03
4H	*Ucp1* qPCR	2 way ANOVA with a Tukey correction for multiple comparisons	MAX: Young vs. Young + Iso	<0.001
			MAX: Aged vs. Aged + Iso	<0.001
			Young + Iso: MIN vs. MAX	<0.001
			Aged + Iso: MIN vs. MAX	<0.001
6E	*Npr3* qPCR	2 way ANOVA with a Tukey correction for multiple comparisons	TN: Young vs. Aged	0.001
			14D: Young vs. Aged	0.01
			Young: TN vs. 14D	0.04
			Aged: TN vs. 3D	0.004

			Aged: TN vs. 14D	0.005
S1A	Body mass	2 way ANOVA with a Tukey correction for multiple comparisons	TN: Young vs. Aged	<0.001
			3D: Young vs. Aged	<0.001
			14D: Young vs. Aged	<0.001
S1B	iWAT mass	2 way ANOVA with a Tukey correction for multiple comparisons	TN: Young vs. Aged	0.005
			3D: Young vs. Aged	0.03
S1B	iWAT mass %	2 way ANOVA with a Tukey correction for multiple comparisons	No comparisons significant	N/A
S1E	*Ucp1* qPCR	2 way ANOVA with an Uncorrected Fisher's LSD	Young: TN vs. 14D	0.01
			Aged: TN vs. 14D	0.008
S1E	*Cidea* qPCR	2 way ANOVA with an Uncorrected Fisher's LSD	No comparisons significant	N/A
S4D	*Npr1* qPCR	2 way ANOVA with a Tukey correction for multiple comparisons	Young: TN vs. 3D	0.03
S4D	*Npr2* qPCR	2 way ANOVA with a Tukey correction for multiple comparisons	No comparisons significant	N/A
S4H	*Acly* qPCR	2 way ANOVA with a Tukey correction for multiple comparisons	3D: Young vs. Aged	<0.001
			14D: Young vs. Aged	<0.001
			Young: TN vs. 3D	<0.001
			Young: TN vs. 14D	<0.001
			Young: 3D vs. 14D	<0.001

724 **References**

725 Amiya Kumar Ghosh, M.O.B., Theresa Mau, Nathan Qi, and Raymond Yung (2019). Adipose
726 Tissue Senescence and Inflammation in Aging is Reversed by the Young Milieu. J Gerontol A
727 Biol Sci Med Sci *74*, 1709-1715.

728 Barreau, C., Labit, E., Guissard, C., Rouquette, J., Boizeau, M.L., Gani Koumassi, S., Carriere,
729 A., Jeanson, Y., Berger-Muller, S., Dromard, C., *et al.* (2016). Regionalization of browning
730 revealed by whole subcutaneous adipose tissue imaging. Obesity (Silver Spring) *24*, 1081-1089.

731 Becher, T., Palanisamy, S., Kramer, D.J., Eljalby, M., Marx, S.J., Wibmer, A.G., Butler, S.D.,
732 Jiang, C.S., Vaughan, R., Schoder, H., *et al.* (2021). Brown adipose tissue is associated with
733 cardiometabolic health. Nat Med *27*, 58-65.

734 Benvie, A.M., Lee, D., Steiner, B.M., Xue, S., Jiang, Y., and Berry, D.C. (2023). Age-dependent
735 Pdgfrbeta signaling drives adipocyte progenitor dysfunction to alter the beige adipogenic niche in
736 male mice. Nat Commun *14*, 1806.

737 Berry, D.C., Jiang, Y., Arpke, R.W., Close, E.L., Uchida, A., Reading, D., Berglund, E.D., Kyba,
738 M., and Graff, J.M. (2017). Cellular Aging Contributes to Failure of Cold-Induced Beige
739 Adipocyte Formation in Old Mice and Humans. Cell Metab *25*, 166-181.

740 Berry, D.C., Jiang, Y., and Graff, J.M. (2016). Mouse strains to study cold-inducible beige
741 progenitors and beige adipocyte formation and function. Nat Commun *7*, 10184.

742 Bordicchia, M., Liu, D., Amri, E.Z., Ailhaud, G., Dessi-Fulgheri, P., Zhang, C., Takahashi, N.,
743 Sarzani, R., and Collins, S. (2012). Cardiac natriuretic peptides act via p38 MAPK to induce the
744 brown fat thermogenic program in mouse and human adipocytes. J Clin Invest *122*, 1022-1036.

745 Brosseau, C., Colas, L., Magnan, A., and Brouard, S. (2018). CD9 Tetraspanin: A New Pathway
746 for the Regulation of Inflammation? Front Immunol *9*, 2316.

747 Burl, R.B., Ramseyer, V.D., Rondini, E.A., Pique-Regi, R., Lee, Y.H., and Granneman, J.G.
748 (2018). Deconstructing Adipogenesis Induced by beta3-Adrenergic Receptor Activation with
749 Single-Cell Expression Profiling. Cell Metab *28*, 300-309 e304.

750 Cannon, B., and Nedergaard, J. (2004). Brown Adipose Tissue: Function and Physiological
751 Significance. Physiology Review *84*, 277–359.

752 Cederberg, A., Gronning, L.M., Ahren, B., Tasken, K., Carlsson, P., and Enerback, S. (2001).
753 FOXC2 is a winged helix gene that counteracts obesity, hypertriglyceridemia, and diet-induced
754 insulin resistance. Cell *106*, 563-573.

755 Chi, J., Wu, Z., Choi, C.H.J., Nguyen, L., Tegegne, S., Ackerman, S.E., Crane, A., Marchildon,
756 F., Tessier-Lavigne, M., and Cohen, P. (2018). Three-Dimensional Adipose Tissue Imaging
757 Reveals Regional Variation in Beige Fat Biogenesis and PRDM16-Dependent Sympathetic
758 Neurite Density. Cell Metab *27*, 226-236 e223.

759 Chouchani, E.T., Kazak, L., and Spiegelman, B.M. (2019). New Advances in Adaptive
760 Thermogenesis: UCP1 and Beyond. Cell Metab *29*, 27-37.

761 Chung, M.I., Bujnis, M., Barkauskas, C.E., Kobayashi, Y., and Hogan, B.L.M. (2018). Niche-
762 mediated BMP/SMAD signaling regulates lung alveolar stem cell proliferation and differentiation.
763 Development *145*.

764 Cohen, P., Levy, J.D., Zhang, Y., Frontini, A., Kolodin, D.P., Svensson, K.J., Lo, J.C., Zeng, X.,
765 Ye, L., Khandekar, M.J., *et al.* (2014). Ablation of PRDM16 and Beige Adipose Causes Metabolic
766 Dysfunction and a Subcutaneous to Visceral Fat Switch. Cell *156*, 304-316.

767 Coue, M., Barquissau, V., Morigny, P., Louche, K., Lefort, C., Mairal, A., Carpene, C., Viguerie,
768 N., Arner, P., Langin, D., *et al.* (2018). Natriuretic peptides promote glucose uptake in a cGMP-
769 dependent manner in human adipocytes. Sci Rep *8*, 1097.

770 Cypess, A.M., Chen, Y.C., Sze, C., Wang, K., English, J., Chan, O., Holman, A.R., Tal, I., Palmer,
771 M.R., Kolodny, G.M., *et al.* (2012). Cold but not sympathomimetics activates human brown
772 adipose tissue in vivo. Proc Natl Acad Sci U S A *109*, 10001-10005.

773 Cypess, A.M., Lehman, S., Williams, G., Tal, I., Rodman, D., Goldfine, A.B., Kuo, F.C., Palmer,
774 E.L., Tseng, Y.H., Doria, A., *et al.* (2009). Identification and importance of brown adipose tissue
775 in adult humans. N Engl J Med *360*, 1509-1517.

776 Dichamp, J., Barreau, C., Guissard, C., Carriere, A., Martinez, Y., Descombes, X., Penicaud, L.,
777 Rouquette, J., Casteilla, L., Plouraboue, F., *et al.* (2019). 3D analysis of the whole subcutaneous
778 adipose tissue reveals a complex spatial network of interconnected lobules with heterogeneous
779 browning ability. Sci Rep *9*, 6684.

780 Drokhlyansky, E., Smillie, C.S., Van Wittenberghe, N., Ericsson, M., Griffin, G.K., Eraslan, G.,
781 Dionne, D., Cuoco, M.S., Goder-Reiser, M.N., Sharova, T., *et al.* (2020). The Human and Mouse
782 Enteric Nervous System at Single-Cell Resolution. Cell *182*, 1606-1622 e1623.

783 Ferrero, R., Rainer, P., and Deplancke, B. (2020). Toward a Consensus View of Mammalian
784 Adipocyte Stem and Progenitor Cell Heterogeneity. Trends Cell Biol *30*, 937-950.

785 Fleming, S.J., Chaffin, M.D., Arduini, A., Akkad, A.-D., Banks, E., Marioni, J.C., Philippakis,
786 A.A., Ellinor, P.T., and Babadi, M. (2022). CellBender remove-background: a deep generative
787 model for unsupervised removal of background noise from scRNA-seq datasets. bioRxiv.

788 Gentili, A., Frangione, M.R., Albini, E., Vacca, C., Ricci, M.A., De Vuono, S., Boni, M., Rondelli,
789 F., Rotelli, L., Lupattelli, G., *et al.* (2017). Modulation of natriuretic peptide receptors in human
790 adipose tissue: molecular mechanisms behind the "natriuretic handicap" in morbidly obese
791 patients. Transl Res *186*, 52-61.

792 Gesta, S., Tseng, Y.H., and Kahn, C.R. (2007). Developmental origin of fat: tracking obesity to its
793 source. Cell *131*, 242-256.

794 Goldberg, E.L., Shchukina, I., Youm, Y.H., Ryu, S., Tsusaka, T., Young, K.C., Camell, C.D.,
795 Dlugos, T., Artyomov, M.N., and Dixit, V.D. (2021). IL-33 causes thermogenic failure in aging
796 by expanding dysfunctional adipose ILC2. Cell Metab *33*, 2277-2287 e2275.

797 Goncalves, L.F., Machado, T.Q., Castro-Pinheiro, C., de Souza, N.G., Oliveira, K.J., and
798 Fernandes-Santos, C. (2017). Ageing is associated with brown adipose tissue remodelling and loss
799 of white fat browning in female C57BL/6 mice. Int J Exp Pathol *98*, 100-108.

800 Graja, A., Garcia-Carrizo, F., Jank, A.M., Gohlke, S., Ambrosi, T.H., Jonas, W., Ussar, S., Kern,
801 M., Schurmann, A., Aleksandrova, K., *et al.* (2018). Loss of periostin occurs in aging adipose
802 tissue of mice and its genetic ablation impairs adipose tissue lipid metabolism. Aging Cell *17*,
803 e12810.

Jaitin, D.A., Adlung, L., Thaiss, C.A., Weiner, A., Li, B., Descamps, H., Lundgren, P., Bleriot, C., Liu, Z., Deczkowska, A., *et al.* (2019). Lipid-Associated Macrophages Control Metabolic Homeostasis in a Trem2-Dependent Manner. Cell *178*, 686-698 e614.

Jespersen, N.Z., Larsen, T.J., Peijs, L., Daugaard, S., Homoe, P., Loft, A., de Jong, J., Mathur, N., Cannon, B., Nedergaard, J., *et al.* (2013). A classical brown adipose tissue mRNA signature partly overlaps with brite in the supraclavicular region of adult humans. Cell Metab *17*, 798-805.

Kovacova, Z., Tharp, W.G., Liu, D., Wei, W., Xie, H., Collins, S., and Pratley, R.E. (2016). Adipose tissue natriuretic peptide receptor expression is related to insulin sensitivity in obesity and diabetes. Obesity (Silver Spring) *24*, 820-828.

Lee, Y.H., Kim, S.N., Kwon, H.J., and Granneman, J.G. (2017). Metabolic heterogeneity of activated beige/brite adipocytes in inguinal adipose tissue. Sci Rep *7*, 39794.

Li, B., Gould, J., Yang, Y., Sarkizova, S., Tabaka, M., Ashenberg, O., Rosen, Y., Slyper, M., Kowalczyk, M.S., Villani, A.C., *et al.* (2020). Cumulus provides cloud-based data analysis for large-scale single-cell and single-nucleus RNA-seq. Nat Methods *17*, 793-798.

Long, J.Z., Svensson, K.J., Tsai, L., Zeng, X., Roh, H.C., Kong, X., Rao, R.R., Lou, J., Lokurkar, I., Baur, W., *et al.* (2014). A smooth muscle-like origin for beige adipocytes. Cell Metab *19*, 810-820.

Marcelin, G., Ferreira, A., Liu, Y., Atlan, M., Aron-Wisnewsky, J., Pelloux, V., Botbol, Y., Ambrosini, M., Fradet, M., Rouault, C., *et al.* (2017). A PDGFRalpha-Mediated Switch toward CD9(high) Adipocyte Progenitors Controls Obesity-Induced Adipose Tissue Fibrosis. Cell Metab *25*, 673-685.

Martinez Calejman, C., Trefely, S., Entwisle, S.W., Luciano, A., Jung, S.M., Hsiao, W., Torres, A., Hung, C.M., Li, H., Snyder, N.W., *et al.* (2020). mTORC2-AKT signaling to ATP-citrate lyase drives brown adipogenesis and de novo lipogenesis. Nat Commun *11*, 575.

McDonald, M.E., Li, C., Bian, H., Smith, B.D., Layne, M.D., and Farmer, S.R. (2015). Myocardin-related transcription factor a regulates conversion of progenitors to beige adipocytes. Cell *160*, 105-118.

Merrick, D., Sakers, A., Irgebay, Z., Okada, C., Calvert, C., Morley, M.P., Percec, I., and Seale, P. (2019). Identification of a mesenchymal progenitor cell hierarchy in adipose tissue. Science *364*.

Moro, C., Galitzky, J., Sengenes, C., Crampes, F., Lafontan, M., and Berlan, M. (2004). Functional and pharmacological characterization of the natriuretic peptide-dependent lipolytic pathway in human fat cells. J Pharmacol Exp Ther *308*, 984-992.

Mottillo, E.P., Balasubramanian, P., Lee, Y.H., Weng, C., Kershaw, E.E., and Granneman, J.G. (2014). Coupling of lipolysis and de novo lipogenesis in brown, beige, and white adipose tissues during chronic beta3-adrenergic receptor activation. J Lipid Res *55*, 2276-2286.

Nguyen, H.P., Lin, F., Yi, D., Xie, Y., Dinh, J., Xue, P., and Sul, H.S. (2021). Aging-dependent regulatory cells emerge in subcutaneous fat to inhibit adipogenesis. Dev Cell *56*, 1437-1451 e1433.

Pfannenberg, C., Werner, M.K., Ripkens, S., Stef, I., Deckert, A., Schmadl, M., Reimold, M., Haring, H.U., Claussen, C.D., and Stefan, N. (2010). Impact of age on the relationships of brown adipose tissue with sex and adiposity in humans. Diabetes *59*, 1789-1793.

845 Prabata, A., Ikeda, K., Rahardini, E.P., Hirata, K.I., and Emoto, N. (2021). GPNMB plays a
846 protective role against obesity-related metabolic disorders by reducing macrophage inflammatory
847 capacity. J Biol Chem *297*, 101232.

848 Rogers, N.H., Landa, A., Park, S., and Smith, R.G. (2012). Aging leads to a programmed loss of
849 brown adipocytes in murine subcutaneous white adipose tissue. Aging cell *11*, 1074-1083.

850 Rosell, M., Kaforou, M., Frontini, A., Okolo, A., Chan, Y.W., Nikolopoulou, E., Millership, S.,
851 Fenech, M.E., MacIntyre, D., Turner, J.O*., et al.* (2014). Brown and white adipose tissues: intrinsic
852 differences in gene expression and response to cold exposure in mice. American journal of
853 physiology Endocrinology and metabolism *306*, E945-964.

854 Rosenwald, M., Perdikari, A., Rulicke, T., and Wolfrum, C. (2013). Bi-directional interconversion
855 of brite and white adipocytes. Nat Cell Biol *15*, 659-667.

856 Saade, M., Araujo de Souza, G., Scavone, C., and Kinoshita, P.F. (2021). The Role of GPNMB in
857 Inflammation. Front Immunol *12*, 674739.

858 Saito, M., Okamatsu-Ogura, Y., Matsushita, M., Watanabe, K., Yoneshiro, T., Nio-Kobayashi, J.,
859 Iwanaga, T., Miyagawa, M., Kameya, T., Nakada, K*., et al.* (2009). High incidence of
860 metabolically active brown adipose tissue in healthy adult humans: effects of cold exposure and
861 adiposity. Diabetes *58*, 1526-1531.

862 Sakers, A., De Siqueira, M.K., Seale, P., and Villanueva, C.J. (2022). Adipose-tissue plasticity in
863 health and disease. Cell *185*, 419-446.

864 Sanchez-Gurmaches, J., Tang, Y., Jespersen, N.Z., Wallace, M., Martinez Calejman, C., Gujja, S.,
865 Li, H., Edwards, Y.J.K., Wolfrum, C., Metallo, C.M*., et al.* (2018). Brown Fat AKT2 Is a Cold-
866 Induced Kinase that Stimulates ChREBP-Mediated De Novo Lipogenesis to Optimize Fuel
867 Storage and Thermogenesis. Cell Metab *27*, 195-209 e196.

868 Seale, P., Conroe, H.M., Estall, J., Kajimura, S., Frontini, A., Ishibashi, J., Cohen, P., Cinti, S.,
869 and Spiegelman, B.M. (2011). Prdm16 determines the thermogenic program of subcutaneous
870 white adipose tissue in mice. J Clin Invest *121*, 96-105.

871 Sengenès, C., Berlan, M., Glisezinski, I., Lafontan, M., and Galitzky, J. (2000). Natriuretic
872 peptides: a new lipolytic pathway in human adipocytes. The FASEB Journal *14*, 1345-1351.

873 Sengenes, C., Bouloumie, A., Hauner, H., Berlan, M., Busse, R., Lafontan, M., and Galitzky, J.
874 (2003). Involvement of a cGMP-dependent pathway in the natriuretic peptide-mediated hormone-
875 sensitive lipase phosphorylation in human adipocytes. J Biol Chem *278*, 48617-48626.

876 Shamsi, F., Piper, M., Ho, L.L., Huang, T.L., Gupta, A., Streets, A., Lynes, M.D., and Tseng, Y.H.
877 (2021). Vascular smooth muscle-derived Trpv1(+) progenitors are a source of cold-induced
878 thermogenic adipocytes. Nat Metab *3*, 485-495.

879 Shao, M., Ishibashi, J., Kusminski, C.M., Wang, Q.A., Hepler, C., Vishvanath, L., MacPherson,
880 K.A., Spurgin, S.B., Sun, K., Holland, W.L*., et al.* (2016). Zfp423 Maintains White Adipocyte
881 Identity through Suppression of the Beige Cell Thermogenic Gene Program. Cell Metab *23*, 1167-
882 1184.

883 Shao, M., Wang, Q.A., Song, A., Vishvanath, L., Busbuso, N.C., Scherer, P.E., and Gupta, R.K.
884 (2019). Cellular Origins of Beige Fat Cells Revisited. Diabetes *68*, 1874-1885.

885 Slyper, M., Porter, C.B.M., Ashenberg, O., Waldman, J., Drokhlyansky, E., Wakiro, I., Smillie,
886 C., Smith-Rosario, G., Wu, J., Dionne, D., *et al.* (2020). A single-cell and single-nucleus RNA-
887 Seq toolbox for fresh and frozen human tumors. Nat Med *26*, 792-802.

888 St-Onge, M.-P. (2005). Relationship between body composition changes and changes in physical
889 function and metabolic risk factors in aging. Current Opinion in Clinical Nutrition and Metabolic
890 Care *8*, 523–528.

891 Stine, R.R., Shapira, S.N., Lim, H.W., Ishibashi, J., Harms, M., Won, K.J., and Seale, P. (2016).
892 EBF2 promotes the recruitment of beige adipocytes in white adipose tissue. Mol Metab *5*, 57-65.

893 Ussar, S., Lee, K.Y., Dankel, S.N., Boucher, J., Haering, M.F., Kleinridders, A., Thomou, T., Xue,
894 R., Macotela, Y., Cypess, A.M., *et al.* (2014). ASC-1, PAT2, and P2RX5 are cell surface markers
895 for white, beige, and brown adipocytes. Sci Transl Med *6*, 247ra103.

896 Wang, Q.A., Tao, C., Gupta, R.K., and Scherer, P.E. (2013). Tracking adipogenesis during white
897 adipose tissue development, expansion and regeneration. Nat Med *19*, 1338-1344.

898 Wang, W., Ishibashi, J., Trefely, S., Shao, M., Cowan, A.J., Sakers, A., Lim, H.W., O'Connor, S.,
899 Doan, M.T., Cohen, P., *et al.* (2019). A PRDM16-Driven Metabolic Signal from Adipocytes
900 Regulates Precursor Cell Fate. Cell Metab *30*, 174-189 e175.

901 Wang, W., and Seale, P. (2016). Control of brown and beige fat development. Nat Rev Mol Cell
902 Biol *17*, 691-702.

903 Wu, J., Bostrom, P., Sparks, L.M., Ye, L., Choi, J.H., Giang, A.H., Khandekar, M., Virtanen, K.A.,
904 Nuutila, P., Schaart, G., *et al.* (2012). Beige adipocytes are a distinct type of thermogenic fat cell
905 in mouse and human. Cell *150*, 366-376.

906 Yoneshiro, T., Aita, S., Matsushita, M., Okamatsu-Ogura, Y., Kameya, T., Kawai, Y., Miyagawa,
907 M., Tsujisaki, M., and Saito, M. (2011). Age-related decrease in cold-activated brown adipose
908 tissue and accumulation of body fat in healthy humans. Obesity (Silver Spring) *19*, 1755-1760.

909 Yu, X.X., Lewin, D.A., Forrest, W., and Adams, S.H. (2002). Cold elicits the simultaneous
910 induction of fatty acid synthesis and beta-oxidation in murine brown adipose tissue: prediction
911 from differential gene expression and confirmation in vivo. FASEB journal : official publication
912 of the Federation of American Societies for Experimental Biology *16*, 155-168.

913 Zheng, G.X., Terry, J.M., Belgrader, P., Ryvkin, P., Bent, Z.W., Wilson, R., Ziraldo, S.B.,
914 Wheeler, T.D., McDermott, G.P., Zhu, J., *et al.* (2017). Massively parallel digital transcriptional
915 profiling of single cells. Nat Commun *8*, 14049.

916